



University of
BRISTOL

DEPARTMENT OF MECHANICAL ENGINEERING

An Investigation of the Ultrasonic Measurement of Static and Dynamic Contact

Pietro E. Carnelli

Supervisor: Prof. B. W. Drinkwater

Report Submitted for the Degree of Engineering June 2013

Acknowledgements

I am extremely thankful to my supervisor and tutor; Prof B.W. Drinkwater, whose knowledge, encouragement and guidance proved invaluable to my project. I would also like to extend my gratitude to Dr J. Zhang for his patience in explaining how to use the micro-topographer and the ultrasonic transducers and to Mr H Bloxham, my project partner, for providing the experimental results used in this report.

Declaration

The accompanying research project report entitled: Investigation of the Ultrasonic Measurement of Static and Dynamic Contact is submitted in the third year of study towards an application for the degree of Master of Engineering in Mechanical Engineering at the University of Bristol. The report is based upon independent work by the candidate. All contributions from others have been acknowledged above. The supervisors are identified at the start of the report. The views expressed within the report are those of the author and not of the University of Bristol.

I hereby declare that the above statements are true.

Signed (author)

.....

Full Name

.....

Date

.....

Declaration of Copyright

Certification of ownership of the copyright in a dissertation presented as part of and in accordance with the requirements for the Final Degree of Master of Engineering at the University of Bristol, Faculty of Engineering.

I hereby assert that I own exclusive copyright in the item named below. I give permission to the University of Bristol Library to add this item to its stock and to make it available for consultation in the library, and for inter-library lending for use in another library. It may be copied in full or in part for any bone fide library or research worker on the understanding that users are made aware of their obligations under the copyright legislation, i.e. that no quotation and no information derived from it may be published without the author's prior consent.

Author	
Title	
Date of Submission	

Signed (author)

.....

Full Name

.....

Date

.....

This dissertation is the property of the University of Bristol Library and may only be used with due regard to the author. Bibliographical references may be noted but no part may be copied for use or quotation in any published work without prior permission of the author. In addition, due acknowledgement for any use must be made

Division of Labour

Pietro Carnelli	Harry Bloxham
Literature and background review of previous projects	
Initial assessment of ultrasonic friction measurement rig	
Background review of ultrasound	
Literature review of static and dynamic, smooth and rough contact models	Literature review of ultrasonic measurement and experimental procedures
Re-design of ultrasonic transducer contacts Re-design of rig top surface	New motor and control system Test piece velocity measurement system New test material attachment system New spring calibration Calibration of test rig Temperature measurement system
New Components Manufacture	
Modelling procedure	Experimental procedure
Static and dynamic modelling results	Static and dynamic experimental results
Analysis of model and experimental results	Analysis of experimental results

I hereby confirm that the table above provides an accurate and fair representation of the allocation of work between project group members.

Signed (author)

.....

Signed (project partner)

.....

Summary

The measurement of the reflection amplitude of ultrasonic waves from a partially contacting static and dynamic solid-solid interface can be used to determine contact conditions. This report investigates the methods and ability of rough static and dynamic contact models to predict ultrasonic wave reflection and interface pressure. A test rig was modified in order to give accurate and repeatable comparisons of ultrasonic reflection data for two interfaces; aluminium-aluminium and aluminium-perspex. Surface profiles of statically and dynamically worn materials were also taken in order to better understand surface conditions at the investigated interfaces. Three surface height distributions; Gaussian, chi-squared and a polynomial curve were developed and fitted to the experimental surface height data. On average the polynomial curve reduced the error (of modelling the surface height data) by half of the next closest distribution; chi-squared. The static rough contact model gave good agreement between experiments and predictions; always within an order of magnitude and in the best case within twenty per cent of the experimental interface pressure and reflection coefficient data. The dynamic slip model predicted an increase of the reflection coefficient between non-slip and dynamic (full slip) conditions. This would suggest that surface roughness changes as the surfaces slip. Results from the surface profiles further highlighted this, as both the root mean square and the mean surface roughness of dynamically worn surfaces were nearly twice the value of the original surfaces before dynamic testing.

Contents

1	INTRODUCTION.....	1
1.1	Ultrasound and Contact Modelling.....	1
1.2	Aims and Objectives.....	2
2	BACKGROUND THEORY AND LITERATURE REVIEW.....	3
2.1	Ultrasound.....	3
2.2	Contact Modelling.....	4
2.3	Ultrasound and Static Rough Contact Modelling.....	7
2.4	Dynamic Rough Contact Modelling.....	10
3	RE-DESIGN OF THE ORIGINAL TEST RIG	12
3.1	Original Test Rig.....	12
3.2	Initial Assessment of the Test Rig.....	13
3.3	Re-Designed Components.....	13
4	EXPERIMENTAL PROCEDURE.....	16
4.1	Surface Profiling.....	16
4.2	Test Rig Experiment.....	16
5	ROUGH CONTACT MODELLING PROCEDURE.....	17
5.1	Static Rough Contact Modelling.....	17
5.2	Dynamic Rough Contact Modelling.....	20
6	DISCUSSION OF RESULTS.....	22
6.1	Finite Element Results.....	22
6.2	Surface Profile and Height Distribution Fitting Results.....	22
6.3	Static Modelling Results.....	26
6.4	Static Modelling Key Parameter Analysis.....	30
6.5	Dynamic Modelling Results	31
7	CONCLUSION.....	33
	REFERENCES.....	34
	APPENDIX.....	37

List of Figures

Figure 2.1. Differences between longitudinal and transverse waves	3
Figure 2.2. Incident, reflected and transmitted waves	4
Figure 2.3. Surface profile example and Hertzian spherical contact model	5
Figure 2.4. Scanning Electron Microscope (SEM) images of aluminium.	6
Figure 2.5. Modified spring model for a partially contacting interface.	9
Figure 2.6. Miller (1978) Coulomb friction model with kinematic locking.	10
Figure 3.1. CAD model of the original rig.....	12
Figure 3.2. CAD model of pivoting threaded clamp contact system	12
Figure 3.3. Acoustic field produced by a 0.25inch, 5MHz longitudinal transducer	15
Figure 3.4. Final design of the new static and dynamic contacts.....	15
Figure 5.1 Flow chart of the surface profile data processing program..	17
Figure 5.2 Coordinate system for the composite surface.....	18
Figure 5.3. Flow chart summarising the Greenwood & Williamson (1996) model.	20
Figure 6.1. Diagram of the punch and the elastic half space.	22
Figure 6.2. PDF Height distribution of statically worn aluminium contacts.	23
Figure 6.3. PDF Height distribution of dynamically worn aluminium contacts.	24
Figure 6.4. Aluminium-Aluminium interface composite surface PDF height distribution.	25
Figure 6.5. Aluminium-PMMA interface composite surface PDF height distribution..	25
Figure 6.6. Error of the fitting distributions.....	26
Figure 6.7. How the misalignment factor , ψ varies with increasing misalignment angle.	27
Figure 6.8. Aluminium-PMMA interace, comparison of experimental and modelling results of interfacial stiffness and nominal contact pressure	27
Figure 6.9. Aluminium-PMMA interface, comparison of experimental and modelling results of reflection coefficient and nominal contact pressure.	28
Figure 6.10. Aluminium-Aluminium interface, comparison of experimental and modelling results of interfacial stiffness and nominal contact pressure.....	29
Figure 6.11. Aluminium-Aluminium interface, comparison of experimental and modelling results of reflection coefficient and nominal contact pressure.....	29
Figure 6.12. Variation of static model results with varying mean asperity diameter	30
Figure 6.13. Variation of static model results with varying equivalent Young's modulus.	31
Figure 6.14. Dynamic slip model of an aluminium-aluminium interface.....	32
Figure A1. Flow chart of the surface profile data collection experimental process..	38
Figure A2. PDF height distribution data for dynamically worn aluminium test plate.....	39
Figure A3. PDF height distribution data for statically worn perspex test plate.....	39
Figure A4. PDF height distribution data for dynamically worn perspex test plate..	40
Figure A5. Moving cylindrical punch schematic	40

1. Introduction

1.1 Ultrasound and Contact Modelling

All material surfaces are covered by miniature asperities of randomly varying diameters and heights. When two of these ‘rough’ surfaces are pressed together by a force, contact occurs between the tallest asperities of the surface roughness. Thus, the actual area of contact between the two surfaces is significantly less than the apparent area of contact. Therefore, the interface pressures experienced at the contacting asperities is considerably higher than the nominal pressure being applied to the two contacting materials (Drinkwater, et al., 1996). In order to better understand static and dynamic rough contact it is necessary to know the real area of contact, the size and distribution of the contacts and how these parameters vary with the applied load.

Ultrasound is propagating high frequency stress/pressure waves in different kinds of media. The term ‘ultrasound’ and ‘ultrasonic’ refer to the regular mechanical movements of particles with a frequency above 20kHz, making the sound inaudible to humans (Halmshaw, 1991). The majority of current ultrasonic non-destructive testing is carried out within the 1-15MHz frequency range (Silk, 1984). This leads to small wavelengths and hence the ability to detect miniature defects within or at boundaries of contacting materials. Ultrasound is essentially impermeable to air; the amplitude of the transmitted ultrasonic wave across a solid-air boundary is less than a thousandth of a per cent of the original incident ultrasonic wave amplitude. Thus, when ultrasound ‘travels’ across a partially contacting boundary, such as that of aluminium and perspex, ultrasound will only be transmitted where the asperities of the two material surfaces are in contact. As the applied force increases, more asperities will be pressed into contact (increasing contact area and reducing air gaps), allowing for more of the ultrasonic wave to be transmitted across the boundary. Therefore, the transmission and reflection coefficients, defined as the proportion of the incident ultrasonic wave being transmitted across and reflected back respectively, can be used to interrogate a partially contacting interface and extract information regarding the degree of contact between the two material surfaces.

Ultrasonic non-destructive methods of analysing materials and structures started in the 1930’s and has since become an essential tool in many industries such as construction, aerospace, shipping, rail and automotive (Drinkwater, 2012). Non-destructive testing can involve the use of ultrasound in order to determine various geometrical aspects of the materials and structure. For example the presence and extent of defects such as poor cure, cracks, porosity and voids (Adams & Drinkwater, 1999) as well as the degree of contact between components can be recorded and estimated.

The project discussed within this report seeks to investigate and attempt to model static and dynamic rough contact between two materials where there is a static and sliding interface. A

static model based upon analytical solutions for contact mechanics as well as experimental data for surface and material properties is developed and compared with experimental results.

Successful investigation and modelling would produce further methods of non-destructive testing (NDT) by allowing components to be assessed in order to determine interface parameters *in situ*. Thus, removing the time consuming and costly need for disassembly of the components.

1.2 Aims and Objectives

This report aims to investigate the effects of static and dynamic contact of two components upon ultrasonic measurement through both experimentation and extensive modelling.

In order achieve these aims a set of objectives were set out:

- Conduct a thorough literature review of smooth and rough static contact models, and dynamic slip rough contact models
- Assess through preliminary experimentation and a brief literature review how to modify and improve the test rig built by Murray, et al., 2012. In order to achieve repeatable and accurate reflection results of ultrasonic waves
- Analyse resulting static contact data in order to compare to rough contact models
- Conduct a series of surface roughness and micro-topography measurements in order to provide accurate inputs for static contact models and comparison of dynamic and static surface conditions
- Compare static contact model results with experimental results

2. Background Theory and Literature Review

2.1 Ultrasound

Ultrasonic Waves

Ultrasound is the propagation of high frequency stress/pressure waves in different materials. Ultrasound can be categorised as either guided or bulk waves. This report focuses on bulk waves since they are able to transmit through a medium and interact with a material boundary. In a solid, bulk waves can be either longitudinal (compressional) or shear (transverse) waves. Longitudinal waves represent a series of collinear displacement and propagation compactions and rarefactions within the material (Silk, 1984). Shear or transverse waves propagate at right angles to their displacement, both wave forms are shown in figure 2.1 below.

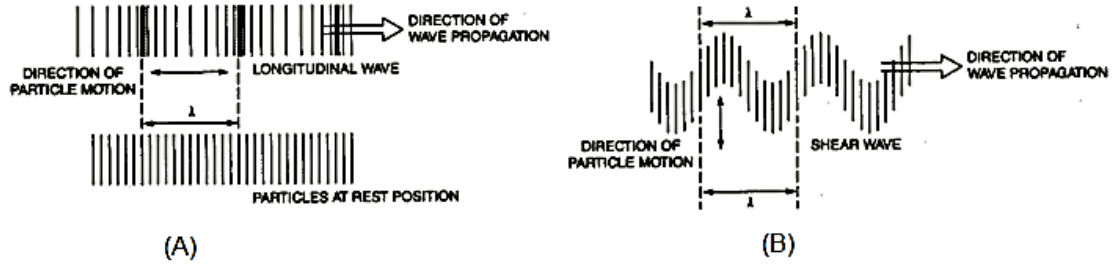


Figure 2.1 Diagram showing (A) longitudinal and (B) transverse waves reproduced from Larson, n.d

The full three dimensional ultrasonic wave equations through a continuous medium are included in appendix A1 for completeness. For the work discussed within this report and due to the type of transducers used in experimentation, only the propagation of normal incidence ultrasonic waves were investigated. Therefore, the full three dimensional wave equations can be simplified into a one dimensional wave equation form, equation 2.1 below,

$$\frac{\partial^2 u}{\partial x^2} = \frac{1}{c^2} \frac{\partial^2 u}{\partial t^2} \quad (2.1)$$

where x is direction being considered, u is the particle displacement, t is time and c is the wave speed. Equation 2.1 can be solved analytically to give the general solution:

$$u = A_1 e^{i(kx - \omega t)} + A_2 e^{-i(kx - \omega t)} \quad (2.2)$$

where, A is the wave amplitude, ω is the wave frequency and $k = \frac{\omega}{c}$ is the wave number.

Reflection Coefficient

Similar to light waves traveling from a different medium to another, some of the incidence ultrasonic wave, u_i , originally transmitted from the transducer is reflected when the wave crosses a boundary between two materials (media) of differing acoustic impedances, Z (the

product of the wave speed, c and the material density, ρ). The greater the difference between material acoustic impedances, the greater the percentage of energy that will be reflected at the interface (boundary) forming a reflected ultrasonic wave, u_r (Gonzalez-Valadez & Dywer-Joyce, 2009). The fraction of the incident wave intensity that is reflected is referred to as the reflection coefficient, RC . This property of ultrasonic waves is shown below in figure 2.2.

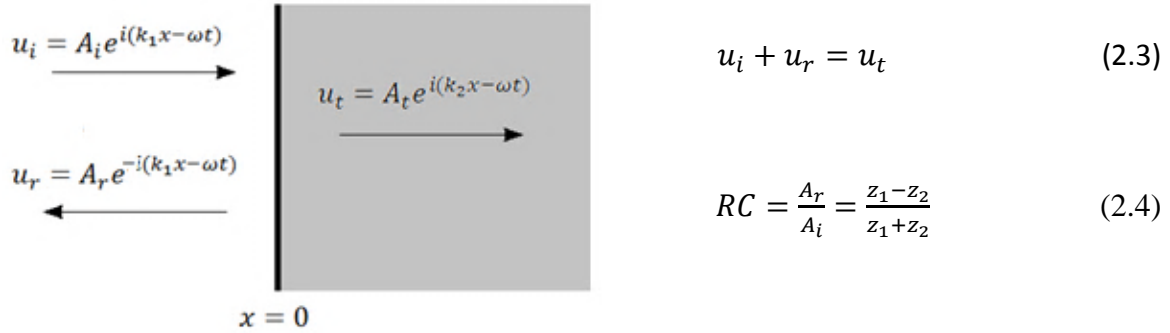


Figure 2.2. Diagram showing the three waves travelling from left to right and normal to the boundary surface represented by the solid line at $x = 0$. u_i, u_r, u_t are the wave displacements for the incident, reflected and transmitted waves respectively. k_1 and k_2 are the wave numbers for the two mediums either side of the boundary

If a closed system is assumed, all the energy of the incident wave is shared between the reflected and transmitted wave (Rose, 1999), leading to equation 2.3 above. The reflection coefficient can then be derived from equation 2.3 with two boundary conditions for stress and displacement (a more detailed derivation is included in appendix A1) resulting in equation 2.4, where Z_1 and Z_2 are the acoustic impedances of each medium either side of the boundary, $x = 0$. A_r and A_i are the amplitudes of the reflected and incident wave respectively.

2.2 Contact Modelling

Smooth Surfaces

Smooth static contact modelling of two elastic bodies with curved surfaces being pressed together was first described and solved analytically by Heinrich Hertz in 1882, with his paper titled “*On the contact of elastic solids*”. Hertz was able to show that if the surfaces in contact were assumed to be frictionless and part of perfectly elastic solids, an ellipsoidal (Hertzian) distribution of contact pressure would produce elastic displacements in the two solids in contact. A typical Hertzian spherical contact is shown in figure 2.3 D below.

In reality surfaces are not smooth (see surface profiles of aluminium and perspex figure 2.3 A below) and hence real cases of smooth contact are extremely rare (Johnson, 1985). The closest known smooth surface found in nature is mica (a group of sheet silicate minerals), which can be cleaved along atomic planes under ‘clean’ laboratory conditions in order to give a surface that is essentially atomically smooth. Mica has been used to obtain nearly ‘perfect’ smooth contact experimental results.

Generally, contact between two solid surfaces is discontinuous and the ‘real’ area of contact is a minute fraction of the ‘nominal’ contact area (Kendall & Tabor, 1971). Even using a lathe to

flatten rough surfaces will be unsuccessful, since serrations will be produced by the lathe machining tool instead.

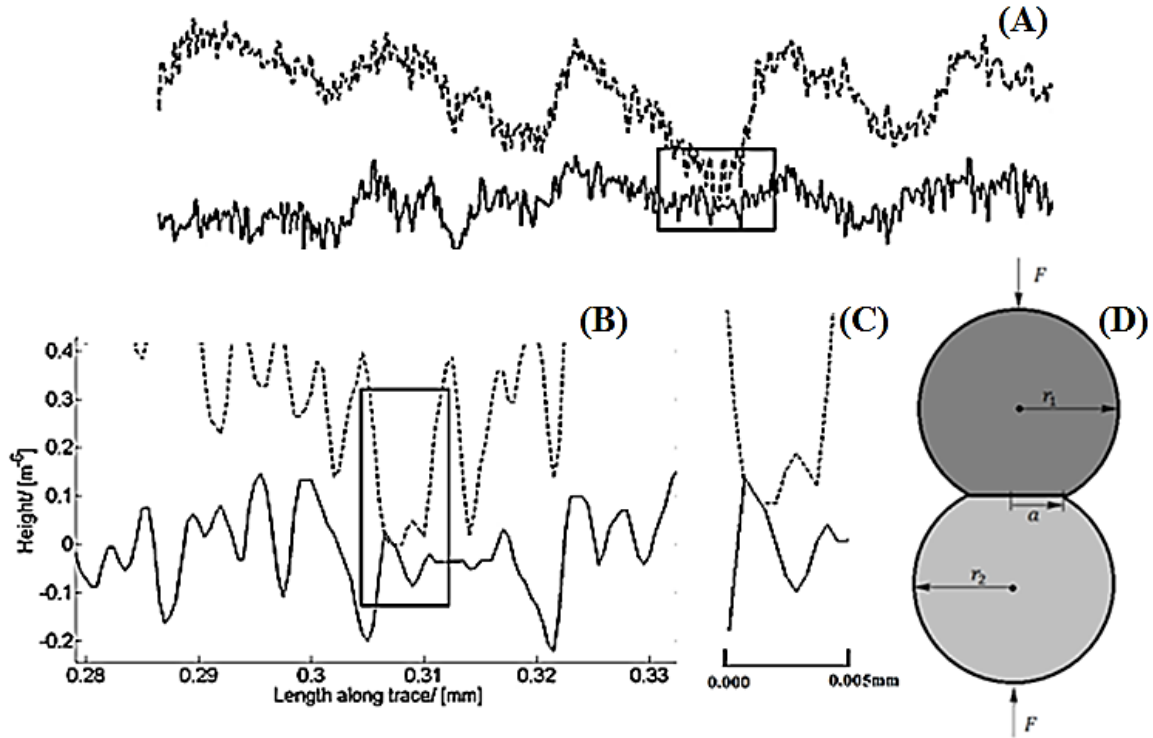


Figure 2.3. (A) Surface profiles (0.5mm lengths) of aluminium contact (dashed) and perspex (solid line). (B) Highlighted and enlarged section of contact, (C) enlargement of highlighted contact section and (D) typical Hertzian contact between two smooth spheres.

Rough Surfaces

As mentioned in the previous section, the real area of contact between two rough surfaces can be minute in comparison to the nominal (perceived) contact area. This is due to the complicated interaction between the asperities from each surface (shown by the surface profiles in figure 2.3). In order to predict the contact pressure between two surfaces, an actual area of contact must be derived or assumed. This is no simple feat due to the fractal nature of surfaces; as they are self-similar at every scale which they are observed in (Carbone, et al., 2009). Therefore, it is almost impossible to determine the actual size of asperities in question and which ones are in contact, as the measurement and number changes depending on the chosen observational length scale. This length scale problem is akin to measuring the length of the coast line of Great Britain or the border between Spain and Portugal. In fact, it can never be properly determined. Since the smaller the measurement length scale used (imagine a person ambling on the ground with a ruler compared to a passenger observing from an aeroplane) the longer the overall measured length; the closer the observer looks the more detail is revealed, thus, donating a larger overall measurement length.

Rough surfaces follow this self-similar pattern when the observer ‘zooms in’ using a normal optical microscope and then a scanning electron microscope (SEM) as shown below in figure 2.4. Therefore in the case of rough surfaces, the measuring length scale ultimately determines

the estimated actual area of contact between the surfaces and consequently the pressure being applied at the interface.

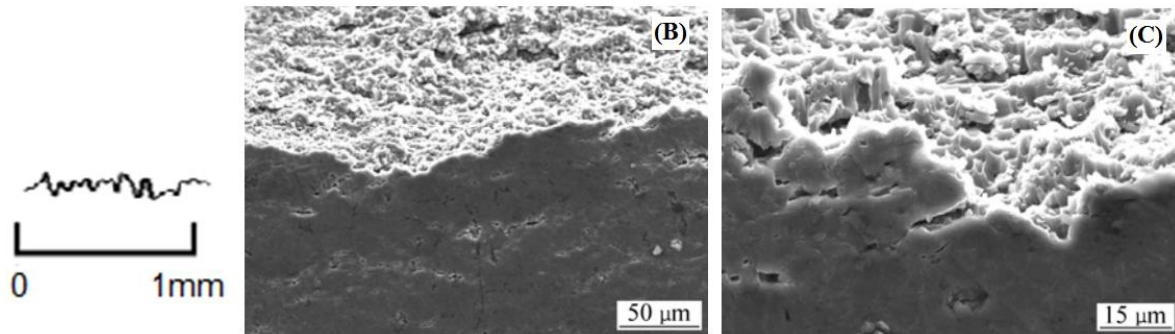


Figure 2.4. (A) Aluminium surface profile from experiment, (B) and (C) SEM images of aluminium 6061 alloy at decreasing length scales reproduced from Wang, et al., 2010. Note the similarity of the surface regardless of the scale it is being viewed at, hence their fractal nature.

As the surface is observed more and more closely, the measured area of contact decreases as the definition between contact and voids gets ever more precise (as more detail is revealed). When taken to the limit in terms of atoms, the contact areas become infinitely small. Therefore, the pressure tends to infinity regardless of the load being applied to the two surfaces. This would immediately suggest that the contact between each asperity is within the plastic deformation region of the material, (since the stresses involved are almost infinite) in reality this is not always observed (Greenwood & Rowe, 1965).

Rough Surface Contact Modelling

A generalized model of rough contact where each asperity is covered with ‘microasperities’ which in turn are covered with ‘micromicroasperities’ was shown to give successively closer approximations to the hypothesis that the real contact area is proportional to the normal load as smaller and smaller asperities were considered (Archard, 1957).

Contact between nominally flat surfaces can be determined by considering a plastic or elastic condition. Historically it was assumed that all asperities deformed plastically, however, it was observed that this was not always the case (Greenwood & Rowe, 1965). As the asperities are crushed the material is actually being locally strain hardened relative to the bulk material. Thus preventing plastic flow, defined as continued deformation with no further increase in stress (Harris, 2005). Furthermore, as the asperities are being crushed by the normal load they are constrained by the presence of adjacent asperities from further deformation (Childs, 1973). Later, rough contact modelling research suggested that for very rough surfaces there will be plastic flow, while for smoother surfaces contact will be mainly elastic (Greenwood & Williamson, 1966).

Greenwood & Williamson (1966) suggested that all surfaces can be modelled as small half-spheres set at different heights. Each height corresponds to the actual asperity heights of the surface of the material being modelled. Asperity heights were considered to be normally and exponentially distributed. Greenwood & Williamson (1966) concluded from experimental

results that for many surfaces the probability density function (PDF) of the heights of the asperities was better modelled as a Gaussian distribution. However, for computation reasons an exponential distribution was also suggested and reasonably modelled the lowermost 75% of the asperities of most surfaces. The Gaussian distribution approximation allowed them to statistically approximate the average number of asperities in contact as a (imaginary) perfectly flat surface is pressed into the (real) rough surface. This can then be related to the contact area and eventually stiffness of the interface. Greenwood & Williamson (1966) demonstrated that the onset of plastic flow is largely dependent on local asperity shape and is relatively insensitive to the applied load.

Later research built upon the Greenwood & Williamson (1966) model suggested that a chi-squared distribution was a better fit to the PDF distribution of asperity heights of measured rough surfaces (Brown & Scholz, 1985). A chi-squared distribution allowed for a level of skewedness of the data, something that by definition the symmetrical Gaussian distribution cannot model. Brown & Scholz (1985) also used a correction factor for the misalignment of the asperities derived by Yamada, et al (1978), as surfaces can never be perfectly aligned such that the forces involved at the contact points are purely normal to the interface as described by Hertz, shown later in figure 6.7.

2.3 Ultrasound and Static Rough Contact Modelling

Measuring the Real Area of Contact

Understanding the nature of rough contact modelling can depend on the measured real area of contact. Methods of directly measuring the real area of contact between two rough surfaces are discussed below:

- i) *Electrical resistance.* This is restricted to metal surfaces and a few non-metallic conductors. It is greatly complicated by the rapid formation of surface oxides which vastly increases the resistivity across the boundary compared to that of the contacting materials (Kendall & Tabor, 1971). Even if the problem of rapidly forming surface oxides were overcome, the contact resistance is not proportional to the inverse of the area of contact.
- ii) *Thermal resistance.* The heat flow across contacting surfaces depends on the ‘spreading-thermal resistance’ of the interface. However, this is a difficult quantity to measure since it is susceptible to global temperatures, and heating metals causes them to creep when loaded therefore affecting the results being measured (Gonzalez-Valadez & Dywer-Joyce, 2009).
- iii) *Optical interference and internal reflection.* Requires materials to be transparent and optical interface measurements are affected by discontinuities a few tens of nanometres high (Kendall & Tabor, 1971).
- iv) *Pressure-sensitive films.* A film is placed in between the two surfaces in question and consists of a thin layer of liquid filled bubbles interposed between two paper sheets. As the applied pressure increases, more bubbles burst, thus producing a stain whose intensity and size is related to the area of contact and therefore contact

pressure at the interface (Pau, et al., 2001). This method is invasive as it requires the dismantling of the joint (contact) in question and is not repeatable (with the same film) and results vary with temperature.

- v) *Ultrasonic waves.* An ultrasonic transducer is placed on one solid, with the face perpendicular to the boundary and the intensity of the incident, reflected and transmitted waves are measured and compared for different surfaces in contact at different pressures. Ultrasonic waves are unaffected by surface oxides and can be used with metal and non-metals (Kendall & Tabor, 1971).

Ultrasound and Partially Contacting Rough Surfaces

As previously mentioned, ultrasound has the ability to transmit across material boundaries. A general reflection coefficient, RC , was derived in terms of the acoustic impedances, Z , of the two contacting materials at a perfect boundary (equation 2.4). Clearly from equation 2.4 when two materials have the same acoustic impedance the reflection coefficient equals zero, implying complete transmission.

In reality, very few material boundaries can be considered ‘perfect’ in the sense that there are few or no voids in between the contacting surfaces. Since surfaces are rough at the microscopic level, solid-solid boundaries have to be considered as partially contacting surfaces. Therefore, even if two of the identical materials are in contact, perfect transmission will not generally occur. The interaction of the ultrasonic wave with the interface becomes more complex and the reflection coefficient cannot be accurately determined from equation 2.4. This is caused by the differences in acoustic impedances of air trapped at the interface and the material used. For example, an aluminium-air boundary has a reflection coefficient of 99.99995% of the amplitude of the incident ultrasonic wave, therefore air can be assumed to be ‘impenetrable’ to ultrasonic waves. Each air gap between the contacting surfaces will scatter the incident ultrasonic wave, whereas waves going through points of contact between the materials will hardly be affected by the interface. The reflected and transmitted acoustic fields will be the net results of many wave-scatter interactions (Drinkwater, et al., 1996).

In order to link rough partially contacting surfaces with the ultrasonic waves travelling across them, several modelling attempts have been made using a combination of springs, dampers, and masses to model the interface between the two partially contacting materials. Kendall & Tabor (1971) used a simple spring model to describe the propagation of ultrasound across stationary and sliding surfaces. This agreed with rough contact models of Greenwood & Williamson (1966) which also used a spring (interfacial stiffness per unit area, K) to describe the elasto-plastic deformation of asperities of a rough interface, see equation 2.5 where u is the deflection at the interface or the approach of the mean lines of the two rough surfaces.

Other methods by Krolkowski & Szczepek (1991) and Baik & Thompson (1984) showed negligible improvements from adding dampers and spring masses (respectively) to the original spring model suggested by Tattersall (1973).

Tattersall (1973) derived an equation relating the interfacial stiffness, K , between the rough contacting materials and the ultrasonic reflection coefficient, RC ,

$$K = -\frac{dP_{nom}}{du} \quad (2.5)$$

$$RC = \frac{Z_1 - Z_2 + j\omega\left(\frac{Z_1 Z_2}{K}\right)}{Z_1 + Z_2 + j\omega\left(\frac{Z_1 Z_2}{K}\right)} \quad (2.6)$$

where $\omega = 2\pi f$ (f , is the frequency of the ultrasonic wave), P_{nom} is the nominal contact pressure given by the applied load divided by the nominal contact area and $j = \sqrt{-1}$.

Note that equation 2.6 suggests that RC is a complex number. The complex part of RC represents the change in phase and amplitude of the ultrasonic wave which can be seen experimentally. Tattersall (1973) also derived an equation relating reflection coefficient to adhesion testing between two rough surfaces. Assuming a thin layer between the rough surfaces, equation 2.7 below relates the amplitude of the reflection coefficient between two rough surfaces of different materials.

$$|RC| = \sqrt{\frac{(\omega Z_1 Z_2)^2 + K^2 (Z_1 - Z_2)^2}{(\omega Z_1 Z_2)^2 + K^2 (Z_1 + Z_2)^2}} \quad (2.7)$$

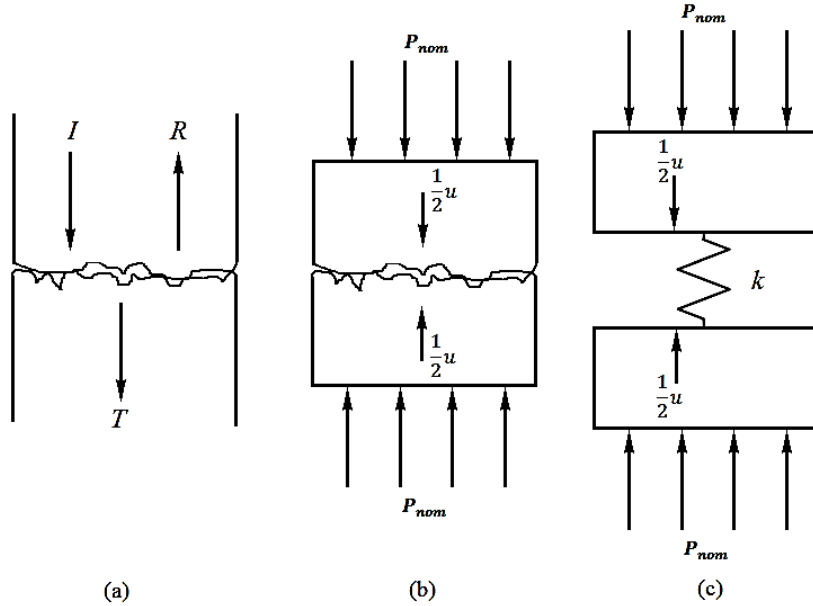


Figure 2.5. Commonly used interfacial stiffness model; (a) the set-up geometry of the contact experiment; (b) the static model of interface; (c) the ultrasonic spring model of the interface used by Drinkwater, et al., (1996), Baltazar, et al., (2002) and Valadez & Dywer-Joyce, (2008).

2.4 Dynamic Rough Contact Modelling

Dynamic contact between smooth and rough surfaces has not been the subject of a lot of research. The effects of a vibrating ultrasonic wave on the contact between asperities have often been ignored by assuming that the amplitudes of the incoming ultrasonic waves were so

small that slip could not be induced at the area of contact (Baltazar, et al., 2002). On the other hand, ultrasonic oscillations have been used to control and reduce friction at sliding interfaces (Teidelt, et al., 2012). It was shown and measured experimentally that the frictional force typically decreases with increasing ultrasonic amplitude and that the decrease in force is larger at smaller sliding velocities. A recent study regarding fretting fatigue attempted to model dynamic contact. A surprising result of the analytical solution was that irrespective of the normal applied pressure at the interface, the rearmost point of a sliding flat punch (shown in figure A5 in the appendix) would never be in contact with the surface of the material below it. In reality this is not always the case, as suggested by the lead author (D. Hills) at a recent research seminar; the model when compared to experiments gave only “*reasonable results*”. This could be due to the roughness of real surfaces suggesting that it was unlikely that there would never be contact at that point.

Dynamic Slip Model

A harmonic shear wave based model of slip at a frictional rough interface has been approximated analytically by Miller (1978). A shortened derivation is included below of the dynamic slip model with Coulomb friction and springs. The springs account for the roughness of the surfaces changing and creating more friction as the asperities are forced together on opposite sides of the interface. The conceptual model for Coulomb friction with springs is shown in figure 2.6.

The model proposed by Miller (1978) consists of a Coulomb friction element of slip stress, τ_s , which itself is a function of the relative displacement across the boundary, y , and its derivative with respect to time, dy/dt . The shearing wave may slide the Coulomb friction element a total distance of $2d$ between the symmetrically positioned springs each of stiffness, k . Therefore, should the amplitude of the incoming shear harmonic wave not exceed the spacing length d then the springs will not be engaged.

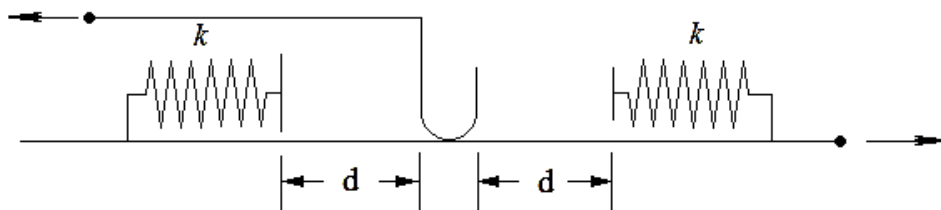


Figure 2.6. Diagram and graph of Miller (1978) Coulomb friction model with horizontal springs.

Dynamic Slip Model Reflection Coefficient

In order to aid the differentiation between static and dynamic contacts, the derivation for the dynamic reflection coefficient is included below.

Starting with the incident ultrasonic wave, u_I

$$u_I = U \sin\left(\frac{\omega x}{c_1} - \omega t\right) \quad (2.9)$$

where $c_i = (\mu_i/\rho_i)^{0.5}$ represents the wave speed in each of the materials either side of the boundary (denoted by the subscripts 1 and 2), U , ω and t are the amplitude, frequency and the time domain respectively.

Replacing the nonlinear frictional stress with a linearized frictional stress such that the resultant boundary stress, τ_F now equals

$$\tau_F \left(y, \frac{dy}{dt} \right) \rightarrow k_e y + c_e \frac{dy}{dt} \quad (2.10)$$

where y , k_e and c_e are the relative displacement across the boundary, equivalent stiffness and damping. The resulting linearized system has a steady-state solution of the form:

$$y(t) = Y \cos(\omega t - \phi) \quad (2.11)$$

Choosing k_e and c_e for minimum mean square differences it may be shown that

$$k_e = \frac{C(Y)}{Y} = \frac{1}{\pi Y} \int_0^{2\pi} \tau_F(Y \cos \theta, -\omega Y \sin \theta) \cos \theta d\theta \quad (2.12)$$

$$c_e = \frac{S(Y)}{Y} = \frac{-1}{\pi Y} \int_0^{2\pi} \tau_F(Y \cos \theta, -\omega Y \sin \theta) \sin \theta d\theta \quad (2.13)$$

And the amplitude-frequency response is

$$C^2(Y) + \left[\frac{\omega \gamma_1 \gamma_2 Y}{\gamma_1 + \gamma_2} - S(Y) \right]^2 = \left[\frac{2\omega \gamma_1 \gamma_2 U}{\gamma_1 + \gamma_2} \right]^2 \quad (2.14)$$

where γ_i , is the square root of the product of the material's shear modulus and density $\gamma_i = (G_i \rho_i)^{0.5}$, $C(Y)$ and $S(Y)$ are defined by the integral equations 2.12 and 2.13. It can be shown that the phase angle, ϕ , is given by

$$\phi = \tan^{-1} \left\{ \left[S(Y) - \frac{\omega \gamma_1 \gamma_2 Y}{\gamma_1 + \gamma_2} \right] / C(Y) \right\} \quad (2.15)$$

and subsequently the reflected wave, u_R is

$$u_R(x, t) = RU \sin \left(\frac{\omega x}{c_1} + \omega t + \phi \right) \quad (2.16)$$

and the reflection coefficient, R is

$$R = \left\{ \left(\frac{Y}{U} \right)^2 \cos^2 \phi + \left[\left(\frac{Y}{U} \right) \sin \phi + \left(\frac{\gamma_1}{\gamma_2} \right) - 1 \right]^2 \right\}^{0.5} \left(\frac{\gamma_1}{\gamma_1 + \gamma_2} \right) \quad (2.17)$$

3. Re-Design of the Original Test Rig

3.1 Original Test Rig

An initial rig designed to aid the investigation of whether or not it was possible to measure friction using ultrasound was provided from a previous year's project, Murray, et al., (2012). Original CAD (Computer Aided Design) models of the rig are shown below in figure 3.1.

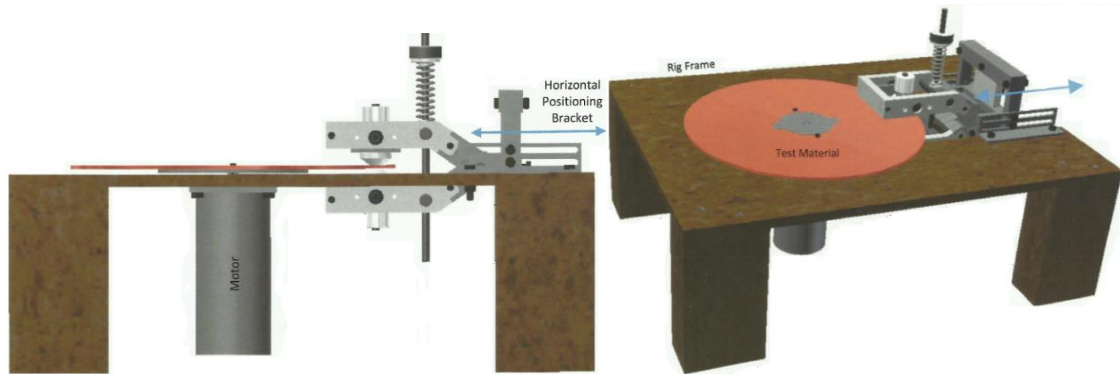


Figure 3.1. CAD model of the entire original rig (Murray, et al., 2012)

The rig originally consisted of four wooden supporting legs, a plywood top surface, a vertically mounted motor, a circular test piece and a two degrees of freedom 'jaw mount' for the two vertically mounted ultrasonic transducers shown below in figure 3.2 A. This allows for a reflection and transmission measurement of the ultrasonic beam passing through the two contacts and the circular test piece. The 'jaw mount' allows for vertical hinged movement and laterally sliding positioning of the transducers. The transducers can be mounted at different radii from the centre of the test piece. The hinged mount for the transducers allows for the aluminium contacts to stay in better vertical contact with the rotating test material piece.

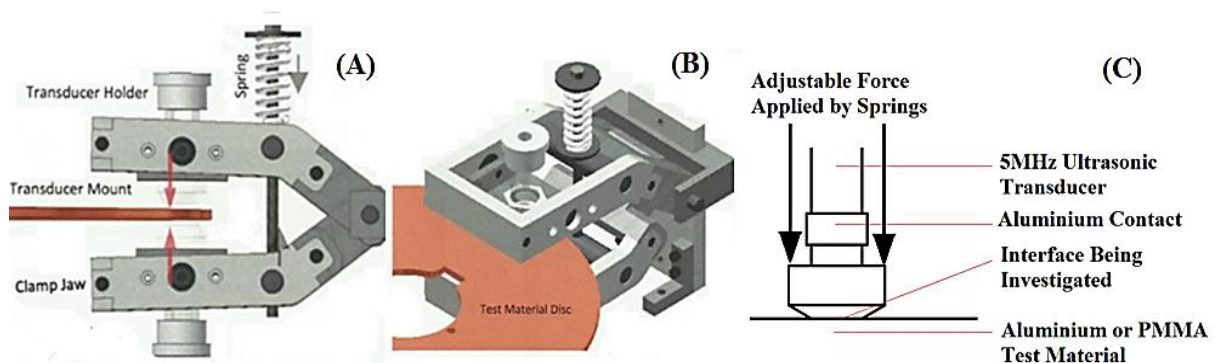


Figure 3.2. (A) and (B) CAD models of the pivoting threaded clamp system used to ensure best alignment of the two contacts with the rotating test material disc. (Murray, et al., 2012). (C) Simplified schematic of the contacting interface being investigated

3.2 Initial Assessment of the Test Rig

Problems from the initial assessment of the test rig are listed below. End initials indicate which person corrected the described problem;

- i) Sagging of the main rig top surface. (PC)
- ii) Rotating plate was badly aligned and in contact with the rig top (HB)
- iii) Motor was not powerful enough to turn test material under full spring load (HB)
- iv) Motor control system was poorly designed and prevented high voltages and currents from being used, limiting the dynamic testing (HB)
- v) Contacts were all worn and not carefully designed (PC)
- vi) Springs were not stiff enough to achieve higher stresses at the interface (HB)

Original Top Surface of Rig

The top surface of the rig was damaged from previous tests. It was immediately clear that the top surface was neither level (parallel to the ground) nor flat. This meant that as the material being tested was rotated certain areas of the plate would come into contact with the top surface of the rig, allowing for poor contact alignment, inducing unnecessary vibrations and causing the motor to slow down when running dynamic experiments.

Causes of the sagging and poor free movement of the rotating plate (the test material) were attributed to poor choice of material for the top surface and location of the supporting legs.

Original Contacts

The original contacts used were heavily worn and had a large surface contact area with the rotating test piece (15mm diameter). The contacts in combination with the original springs provided only 1.13MPa (Murray, et al., 2012) of average contact pressure and from our initial testing the motor struggled to turn the test material at around 0.8MPa, both reducing the range of obtainable static and dynamic results.

3.3 Re-Designed Components

New Top surface of Rig

A re-design of the top surface involved measuring all the various equipment mounting positions (since the original design drawings were unavailable) and repositioning of the supporting legs closer to the heavy motor and transducer mount (with added washers where necessary to ensure a level surface). MDF was chosen as the material for the rig top since it was relatively inexpensive and could be manufactured in one single process with the laser cutter in the faculty workshop. Note that a thicker (9mm) board was used than the previous (6mm) to further prevent sagging, the final design drawing is included in appendix A5.

New Contacts

A new set of contacts needed to be designed and manufactured in order to replace the current worn ones. In order to design an ultrasonic contact, several considerations had to be made

with regards to material, shape and attachment system to the rig. Requirements of the new ultrasonic contacts are listed below:

- i) Low loss of ultrasonic signal
- ii) Prevent internally reflected ultrasonic waves from interfering with measurement
- iii) Allow for a greater interface pressure
- iv) Give good dynamic and static ultrasonic measurements
- v) Inexpensive
- vi) Simple to manufacture, easily repeatable
- vii) Straightforward to attach to the current rig (no unnecessary modifications)

Table 3.2 below, summarises the various properties and the material selection process for the ultrasonic contact. Each variable is given a value ranging from one to ten, with ten being the most desirable value for that particular aspect. A weighting value is multiplied to each score before they are combined to give an overall score for each material.

Table 3.2 Material selection process for ultrasonic contact.

	Weighting	Ultrasonic Contact Material		
		Rexolite®	Aluminium	Perspex
Cost	0.2	1	10	7
Ease of Manufacturing	0.15	5	8	6
Permeability of Sound Waves	0.25	7	9	4
Stiffness	0.25	4	7	3
Wear resistant	0.15	6	7	4
Total	1	4.6	8.25	4.65

Aluminium was deemed the most suitable material for the ultrasonic contact since it was inexpensive to obtain (material was already stocked by the faculty workshop), has a reasonably low acoustic impedance, simple to manufacture the parts on a lathe (the process is repeatable for when more contacts are needed) and it is very stiff (the top part of the contact will not deform under load) and is more scratch resistant than Rexolite® and PMMA.

New Contact Final Design

The new contacts needed to have a smaller diameter, as this allows for a more focused higher energy beam as well as allowing for a greater interface pressure. Figure 3.3 (below) shows how the energy of an emitted ultrasonic beam changes with distance from the emitting ultrasonic transducer's end (centre placed at 0 on the horizontal axis). The results suggest that there is a focusing of the beam at approximately 20mm vertically upwards from where the transducer was mounted.

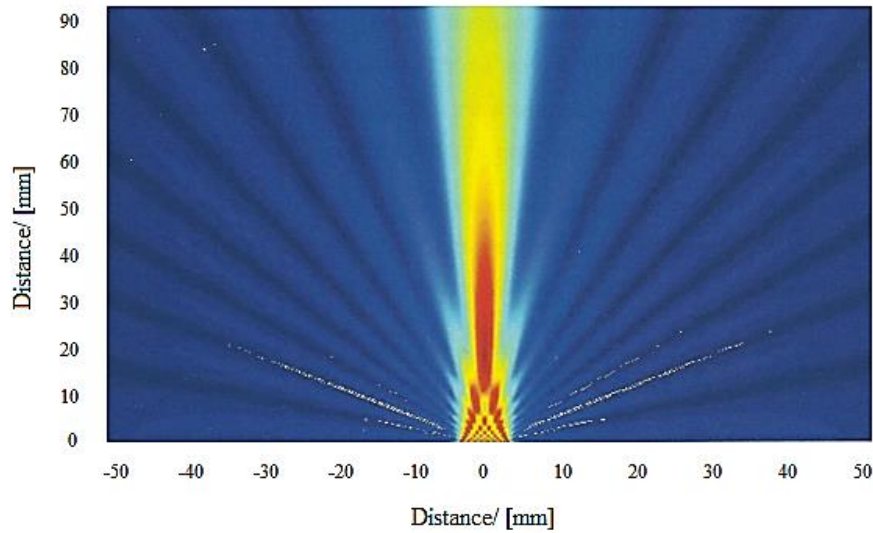


Figure 3.3. Graph showing the field produced by a 0.25inch, 5MHz transducer propagating at 4000ms^{-1} . Colours show energy of the beam, in decreasing order of energy: red, yellow and blue (Murray, et al., 2012).

Therefore the new contacts should be between 20-35mm in length in order that the high energy focused beam would be close to the two contacting interfaces being investigated. A schematic of the final contact used is shown below in figure 3.4 A. The contacts have angled edges to help dynamic testing (prevents contacts from ‘digging into’ the rotating test material) and to prevent internally reflected parts of the ultrasonic beam from disturbing the propagation of the ‘clean’ signal shown below in figure 3.4 B. This reduces the noise at the interface being investigated. The same thread design was cut with a lathe to ensure all contacts were compatible with the test rig mounts. The design drawing of the final contacts used is included in appendix A5.

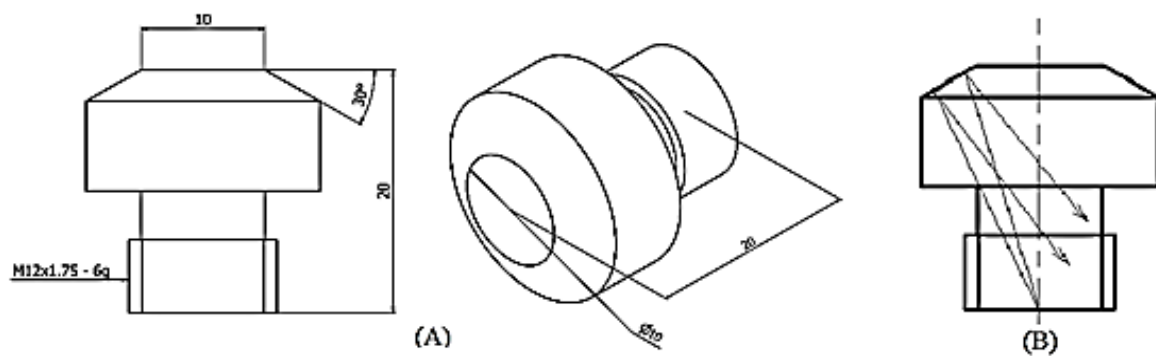


Figure 3.4. (A) Schematic showing final design of the new static and dynamic contacts that were used in this report. All dimensions are in millimetres. (B) Internal reflection of ‘unwanted’ ultrasonic waves (arrows) at the air/aluminium boundary allowing for a ‘clean’ signal at the interface.

4. Experimental Procedure

4.1 Surface Profiling

In order to obtain the most accurate surface data for modelling of rough contact, surface profiles of different materials had to be recorded. The various contact models described by Greenwood & Willamson (1966), Brown & Scholz (1985) and Baltazar et al (2002) all rely on accurate surface profile data, such as the root mean square of heights, average heights and maximum heights of the data. They also rely on accurate representation of the probability distribution function describing the overall heights recorded from the surface data.

Procedure

The surface profiles and roughness measurements were carried out using a Form TalySurf 50 surface profiler (manufactured by Taylor Hobson Precision Ltd.) with a trace speed of 1mm/s, a vertical resolution of 6nm and a spacing between each height measurement of 0.5 μ m.

Statistical randomness of the surface profiles measured was verified by performing several (around ten) measurements of each of the statically and dynamically worn cases of aluminium and perspex in varying directions and locations on the surface area being investigated. For every case, ten different 'paths' along the material were performed and repeated to improve legitimacy of the recorded results, a flow chart showing the process is included in appendix A2 for completeness.

The term 'worn' implies that the contact and plate had been used for static or dynamic testing. Static contacts were used for a couple minutes at increasing nominal pressures whilst ultrasonic measurements were taken. Similarly for dynamically 'worn' contacts, they were run on the rig for a couple of minutes at increasing nominal pressures.

4.2 Test Rig Experiment

Static Measurements

Before the experiments were conducted, the new springs were calibrated in order to be able to accurately determine the pressure being applied to the interface from the compressed length.

The rig was installed with either the aluminium or perspex (Polymethylmethacrylate, PMMA) test plates. Ultrasonic measurements (the reflection coefficient) were taken at equal intervals of increased nominal pressure until a maximum of 4.2MPa was reached. This was repeated several times for both interface conditions on different areas of the test plate with different aluminium contacts.

5. Rough Contact Modelling Procedure

5.1 Static Rough Contact Modelling

Experimental Data Processing For Rough Static Contact Model

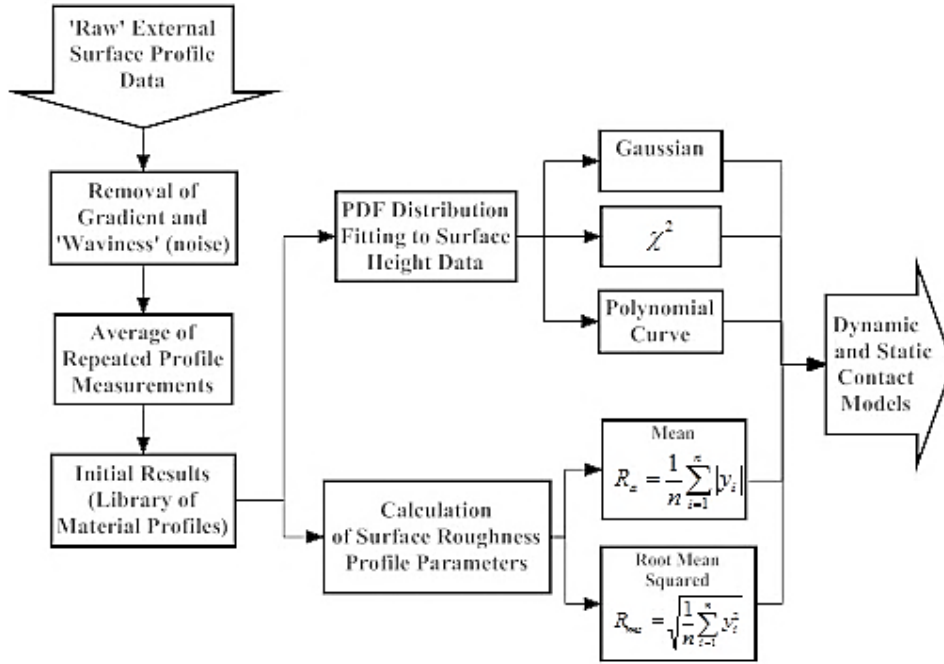


Figure 5.1 Flow chart of the surface profile data processing program. The raw surface profile data was imported into MATLAB® (Version R2012a, MathWorks, Inc) from a .txt file and PDF distributions were fitted to the data and surface parameters were obtained from the data and later used in the static and dynamic contact models.

Rough Static Contact Modelling Assumptions

A brief explanation of the various modelling assumptions introduced by Greenwood & Williamson (1966) and used in this project to model rough contact are listed below:

- i) *All asperities have the same radius of curvature, β .* As discussed in the previous section, measuring asperity diameters is no simple feat due to the fractal nature of rough surfaces (see figure 2.4). However, it is necessary to assume a value for the model and initially the horizontal spacing ($0.5\mu m$) of the surface profiler was chosen as the asperity diameter. Later different values were assumed.
- ii) *Asperity heights vary randomly.* This assumption differentiates the model from previous attempts of modelling rough surfaces as regular sinusoidal waves.
- iii) *The probability that a particular asperity (of the composite surface) has a height between z_c and $z_c + dz_c$ above some reference plane, ∂ , will be $\phi(z_c)dz_c$.* This is the statistical side of the model, where a fitted PDF is assumed and used to

evaluate the number of asperities in contact and later the nominal contact pressure and interfacial stiffness.

- iv) *Asperities do not interact with each other as they are deformed.* A valid assumption in most cases since contact at the low nominal contact pressures being modelled (less than 4.2MPa) will not greatly affect the rough surface since most of the deformation is expected to be elastic.
- v) *The behaviour of an individual asperity is governed by the Hertzian equations.* A valid assumption when applied to small asperities locally at the small length scales being considered.
- vi) *Surface profiles are taken in enough different directions allowing a three dimensional 'isotropic' surface assumption.* Surface profiles of the test materials and contacts were taken in many directions and positions along the test surfaces. This assumption was shown to be reasonably valid by Baltazar, et al., (2002) and Brown & Scholz (1985).

Composite Rough Surfaces

The surface profiles were analysed in order to obtain the relevant surface parameters and PDF distributions. In order to apply the Greenwood & Williamson (1966) model with the various corrections by Baltazar, et al., (2002) and Brown & Scholz (1985), a composite surface was created by combining the two chosen surfaces together following equation (5.1) below,

$$z_s = Q_1 + Q_2 \quad (5.1)$$

where Q_1 and Q_2 are the heights of each surface about a mean reference line. To convert the surfaces to the coordinate system used by Baltazar, et al., (2002) the following equation (5.2)

$$z_c = z_{max} - z_s \quad (5.2)$$

was used where z_{max} is the maximum height of the composite surface z_s . The coordinate system used by Baltazar, et al., (2002) of the composite surface is shown below in figure 5.2.

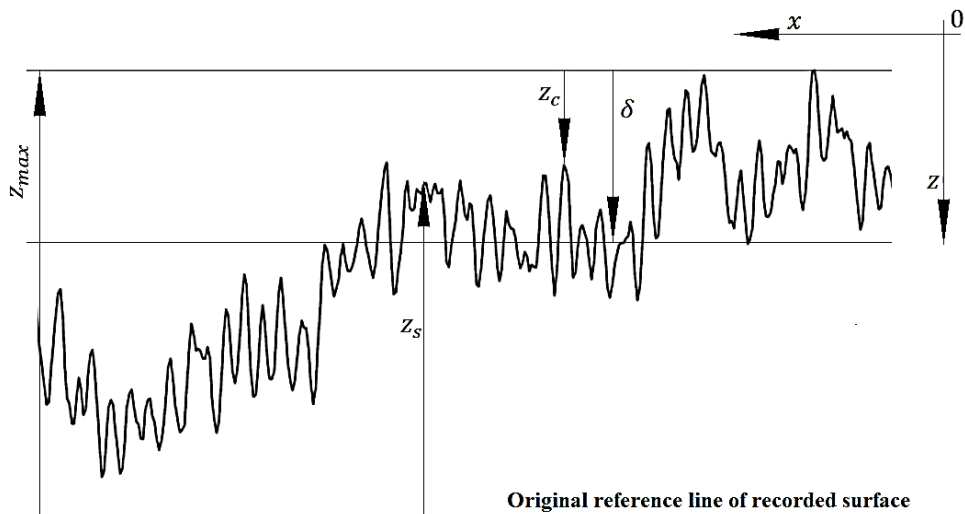


Figure 5.2 Coordinate system for the composite surface, z_c given by equation 5.2.

The composite surface is necessary since it allows for the determination of the asperities in contact as the two real rough surfaces are pressed together. The composite surface allows for the use of a moving flat reference plane denoted by δ . As shown in figure 5.2 above, δ varies from the highest peak, z_{max} to the lowest trough of the composite surface. This is the same as the two real surfaces being pressed together, since by definition z_{max} is the addition of the two highest points of the two surfaces and is where they will contact first. Hence, it's the point where the reference plane δ starts moving downwards. As δ gets larger, more and more asperities will be above it, meaning that more asperities of the two surfaces are in contact.

Composite Material Properties

To accurately model the composite surface, z_c , an equivalent Young's modulus, E' , and shear modulus, G' , were evaluated from the properties of the original materials in contact. This is given by equation 5.3 below,

$$E' = \left(\frac{1-v_1^2}{E_1} + \frac{1-v_2^2}{E_2} \right)^{-1} \quad \text{and} \quad G' = \left(\frac{2-v_1}{G_1} + \frac{2-v_2}{G_2} \right)^{-1} \quad (5.3)$$

where E_1, E_2, G_1, G_2, v_1 and v_2 are the Young's modulus, shear modulus and Poisson's ratios respectively of each of the two contacting materials (denoted by their subscripts).

Normal Pressure and Normal Interfacial Stiffness

The following integral equations 5.4 and 5.5 below were introduced by Greenwood & Williamson (1966), later used by Baltazar, et al., (2002) and Brown & Scholz (1985) to evaluate the normal nominal contact pressure, P , and interfacial stiffness, K , of the interface,

$$P(\delta) = \frac{4}{3} M \psi \int_0^\delta (\delta - z_c)^{1.5} \varphi(z_c) dz_c \quad (5.4)$$

$$K(\delta) = 2M \psi \int_0^\delta (\delta - z_c)^{0.5} \varphi(z_c) dz_c \quad (5.5)$$

where $\varphi(z_c)$ is the fitted distribution; normal, chi squared and polynomial curve (equations of the distributions used are given in appendix A3). δ is the reference plane height which varies from the maximum to the minimum values of the heights of the composite surface z_c . M is a constant consisting of the products of the surface and material parameters and the asperity misalignment correction factor, ψ , and are defined in equations 5.6 and 5.7 respectively,

$$M = \eta E' \beta^{0.5} \quad (5.6)$$

where η , is the summit density, E' , is the equivalent Young's modulus (see equation 5.3) and β is the radius of curvature of the composite peaks. Equation 5.7 below gives the asperity misalignment correction factor introduced by Yamada, et al., (1978) and used by Brown & Scholz (1985) in terms of the angle, χ , which is the point of contact between the two asperities relative to their centre points (see figure 2.4).

$$\psi = \cos^{2.5} \chi + \frac{6G'}{E'} \cos^{0.5} \chi \sin^2 \chi \quad (5.7)$$

A summary model flow chart is shown in figure 5.3 below of the modelling process. The program was developed in MATLAB[®] and used extensively for this report. On the left hand side the inputs are from the data processing program described in figure 5.1 and from data sheets regarding material properties. The asperity density is a function of the chosen asperity diameter and the dimensions of the contact being investigated. The inputs are combined to form the constant M (equation 5.6) and the two integral equations for nominal contact pressure and interfacial stiffness (equations 5.4 and 5.5). The interfacial stiffness, K , is converted to a reflection coefficient, RC , (using equation 2.7) in order to compare with experimental results.

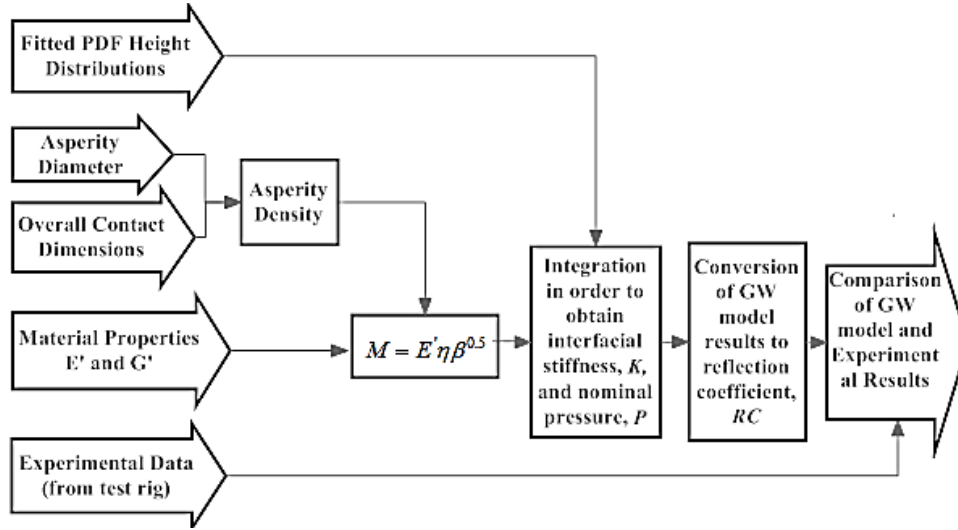


Figure 5.3. Flow chart summarising the modified Greenwood & Williamson (1996) model used in this report.

5.2 Dynamic Rough Contact Modelling

Aluminium-Aluminium Interface

Since the two materials at the interface are identical, therefore,

$$\gamma = \gamma_1 = (\mu_1 \rho_1)^{0.5} = \gamma_2 = (\mu_2 \rho_2)^{0.5} \quad (5.8)$$

The reflection coefficient can be determined from equation 2.17 and can be simplified using the above assumption of identical material properties, and trigonometric identities,

$$\begin{aligned}
 R &= \left\{ \left(\frac{\gamma}{U} \right)^2 \cos^2 \phi + \left[\left(\frac{\gamma}{U} \right) \sin \phi + \left(\frac{\gamma}{\gamma} \right) - 1 \right]^2 \right\}^{0.5} \left(\frac{\gamma}{2\gamma} \right) \\
 R &= \frac{1}{2} \left\{ \left(\frac{\gamma}{U} \right)^2 \cos^2 \phi + \left(\frac{\gamma}{U} \right)^2 \sin^2 \phi \right\}^{0.5} \\
 R &= \frac{1}{2} \left\{ \left(\frac{\gamma}{U} \right)^2 \right\}^{0.5} = \frac{1}{2} \frac{\gamma}{U}
 \end{aligned} \quad (5.9)$$

where R is the reflection coefficient, Y is defined by equation 2.14 and U is the varying amplitude of the shear wave.

First Case, $Y \leq d$

From the results of evaluating the integrals in equations 2.12 and 2.13, $C(Y) = 0$, $S(Y) = -4\tau_s/\pi$ and an substituting back into equation 2.14 gives equation 5.10 below

$$\left[\frac{\omega\gamma^2 Y}{2\gamma} + \frac{4\tau_s}{\pi} \right]^2 = \left[\frac{2\omega\gamma^2 U}{2\gamma} \right]^2$$

$$\text{for } Y \leq d, Y = \pm 2U - \frac{8\tau_s}{\pi\omega\gamma} \quad (5.10)$$

Second Case, $Y > d$

Similarly to the previous case, the results of evaluating the integrals in equations 2.12 and 2.13 gives,

$$C(Y) = 2k/\pi \left\{ \cos^{-1}(d/Y) - 0.5 \sin \left(2 \cos^{-1}(d/Y) \right) \right\} \text{ and } S(Y) = -4\tau_s/\pi$$

and substituting the above results into equation 2.14 gives equation 5.11 below,

$$\left[\frac{2k}{\pi} Y \left\{ \cos^{-1}(d/Y) - 0.5 \sin \left(2 \cos^{-1}(d/Y) \right) \right\} \right]^2 + \left[\frac{\omega\gamma Y}{2} + \frac{4\tau_s}{\pi} \right]^2 - [\omega\gamma U]^2 = 0 \quad (5.11)$$

for clarity, let $a = \frac{\omega\gamma}{2}$, $b = \frac{4\tau_s}{\pi}$, therefore equation 5.11 can be re-written as

$$(C^2(Y) + a^2)Y^2 + 2abY + b^2 - 2aU^2 = 0 \quad (5.12)$$

and then re-arranged to give

$$Y = \frac{-2ab \pm \sqrt{(2ab)^2 - 4(C(Y)^2 + a^2)(b^2 - 4a^2U^2)}}{2(C(Y)^2 + a^2)} \quad (5.13)$$

Solving for Y and substituting the two equations 5.13 and 5.10 into 5.9 would give a value for the reflection coefficient in terms of the displacement. Since 5.13 is non-linear, an approximate solution for Y was obtained through a numerical re-arrangement method of equation 5.12 in order to obtain a value of Y , for every value of ultrasonic shearing wave of amplitude, U . Equations used to generate results are included in the appendix section A3 for completeness. The reflection coefficient was then obtained by substituting the numerical results and chosen values for Y and U respectively into equation 5.9.

6. Discussion of Results

6.1 Finite Element (FE) Results

In order to record as accurate results as possible, a correction factor was applied to all experimental measurements taken from the test rig. Khadem & O'Connor (1969) showed that the pressure distribution at the interface between an elastic block (a cylindrical punch, figure 6.1 A) and an elastic half space is not uniform (see solid line result in figure 6.1 B). In fact the distribution has peaks tending towards infinity at the edges of the cylindrical punch. Two FE packages; Autodesk® Inventor® Professional (Version 2012, Autodesk, Inc.) and Abaqus FEA® (Version 6.12, ABAQUS, Inc.) were used to verify this result and are shown below in figure 6.1 B, dotted and dashed lines respectively. The vertical axis is the ratio of the absolute contact pressure and the nominal pressure applied to the cylindrical punch and the horizontal axis is the ratio of the distance from the centre and the overall radius of the cylindrical punch. Note that for most of the distance (up to 65-70% of the horizontal radius) along the interface the pressure is roughly 79-80% (mean of all three graphs) of the applied nominal pressure at the top of the cylindrical punch. A correction factor of 79.5% is therefore applied to nominal pressure measurements taken from the rig when compared later with the modelling results, as this better represents the true interface pressure being modelled at the interface.

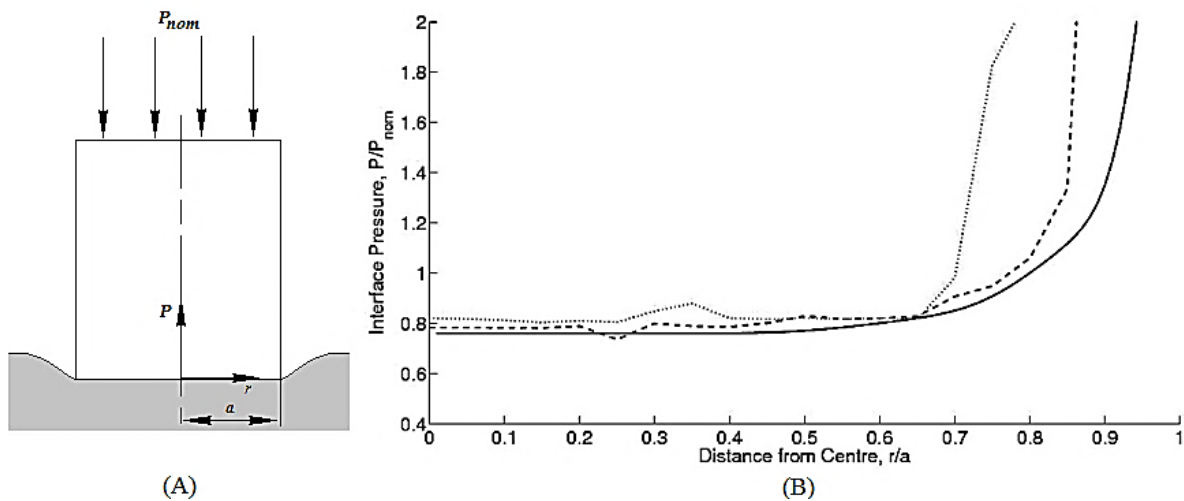


Figure 6.1. (A) Diagram of the punch and the elastic half space (grey area) considered and modelled by Khadem & O'Connor (1969) and the current system being modelled. (B) graph showing the results of two FE modelling techniques; Autodesk® Inventor® Professional 2012 (dotted line, author), Abaqus FEA® (dashed line) (Butler, et al., 2011) and the analytical result (solid line) (Khadem & O'Connor, 1969).

6.2 Surface Profile and Height Distribution Fitting Results

To aid the investigation of dynamic and static contact and the subsequent attempts to model them, a series of surface profiles were taken (see previous section and figure 5.1 for the method used) and the height distributions, PDF's, are shown below. This allows for a more detailed understanding of the differences between dynamic and static interfaces.

Absolute surface height data was collected in a pre-determined set of ‘bins’ (150 was chosen for all figures shown) and then divided by the total number of data points (2000 per 1mm of measured surface profile) to obtain an approximate probability of a chosen height being within a defined boundary. All fitting distributions have been filtered and padded out with zeros when necessary to avoid predictions of negative probability. This was in the minority of cases with some of the polynomial curves fitted to the data.

Three distributions; chi squared (dashed line), Gaussian (dotted line) and a polynomial curve (of order fifteen, solid line) were fitted to the surface height data for comparison, since a function was needed in order to perform the required integrals to obtain nominal contact pressures and stiffnesses (see equations 5.4 and 5.5). Along the horizontal axis (actual) absolute error is plotted for each of the fitted distributions following the same line styling convention of the three distributions but with thinner widths.

Aluminium Contacts

The height distribution of the re-designed aluminium contacts are shown below in figure 6.2. For conciseness results of the ‘brand new’ surfaces are not shown below as they are very similar to the ‘statically worn’ results and are unrepresentative of the more worn contact surfaces used in the experiment. This was mainly due to the low nominal contact (interface) pressures achieved by the test rig (maximum was below 4.5MPa) hence there was little plastic asperity deformation when loaded for a couple of minutes statically to obtain the ultrasonic measurements. As described earlier, three distributions have been fitted and the absolute errors of each are plotted (thinner lines along the bottom of the horizontal axis). All three distributions manage to fit the data reasonably well. The Gaussian distribution had the most error as it over-estimates the height data and is symmetrical by definition, reducing its ability to approximate the tail ends.

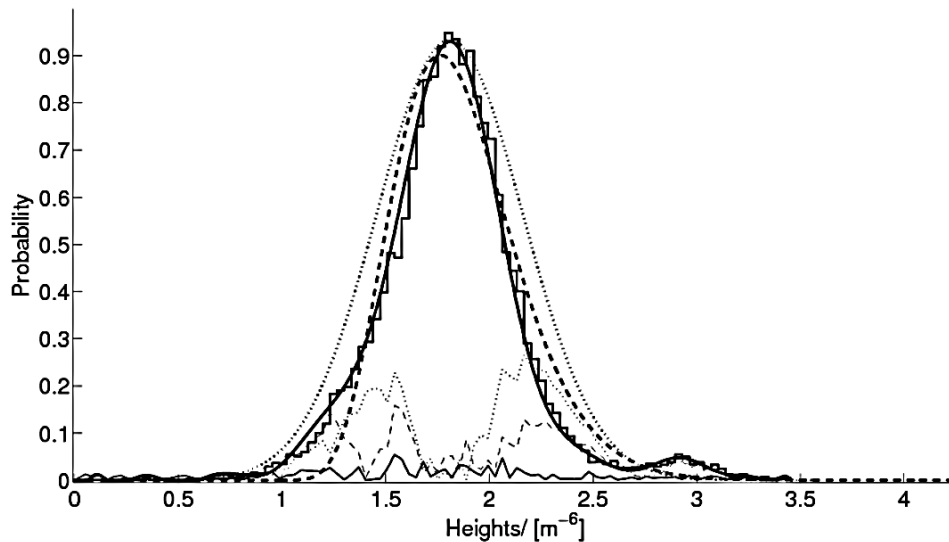


Figure 6.2. PDF of the height distribution of statically worn aluminium contact. Thicker solid, dashed and dotted lines are the polynomial curve, chi-squared and Gaussian distributions respectively. The thinner lines represent the absolute error of each of the distributions with respect to the actual collect height data.

Figure 6.3 below shows the height distribution data for a dynamically worn (used) aluminium contact. It is clear that none of the commonly used statistical distributions such as the Gaussian (dotted line) and chi-squared (dashed line) fit the data at all (see error plots along the horizontal axis). The surface height distribution has two distinct peaks and the range of the measured heights is smaller ($2.5\mu\text{m}$) compared to the statically used contact height range ($3.5\mu\text{m}$). Reasons for this 'extra' peak could include the more anisotropic nature of the surface as well as the fact that taller asperities have been plastically deformed, and even sheared off as the material plate was rotating. Both reasons could be valid as after running the test rig it was noted that a small collection of 'dust' had formed around the contact (especially its leading edge). This suggests that both the material test plate and the contacts were deforming to the point of shearing off material. Further examination of the region of contact of the test plate and the aluminium contacts themselves suggested that small ridges had formed, adding a lot of large scale (low frequency) 'waviness' to the surface profiles.

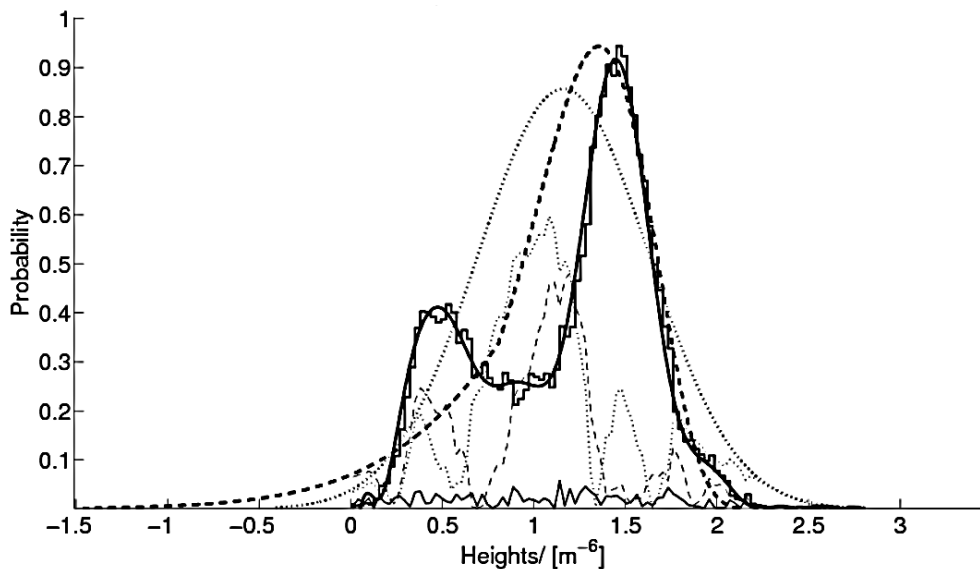


Figure 6.3. Height distribution data for dynamically used aluminium contacts. Thicker solid, dashed and dotted lines are the polynomial curve, chi-squared and Gaussian distributions respectively, the thinner lines represent the absolute error of each of the distributions with respect to the actual collect height data.

Test Plate Materials: Aluminium

Both the contacts and the aluminium disc were made from the same aluminium (6082t6 alloy) and finished in the same way, such that they resulted in similar surface height distributions. Similarly to the surface height distribution for the dynamically worn contacts, two peaks seem to be emerging (figure A2), however, not as clear as witnessed in figure 6.3. As with previous dynamically worn surfaces none of commonly used statistical distributions fit the data well. The polynomial curve best fits the data but fails to fit the highest points.

Test Plate Materials: Perspex

Statically and dynamically worn perspex surface height distributions are included in appendix A4 for completeness. For the static case, all three distributions fitted the surface height data rather well and follows a developing trend throughout all surface height distributions; the

polynomial curve fits the data best, followed by the chi-squared distribution used by Baltazar, et al., 2002 (and originally introduced in more complicated form by Brown & Scholz (1985)) and finally the Gaussian distributions suggested by Greenwood & Williamson (1966). This trend is further analysed later (see figure 6.6).

Composite Surfaces

In order to model the two interfaces being considered, composite surfaces had to be created using the process described in the modelling procedure section (see equations 5.1 and 5.2). The two composite surface height distributions are shown below in figures 6.4 and 6.5. In both cases the polynomial curve best fits the data as it manages to include the most common height values as well as modelling the trailing ends, something that the Gaussian distributions fails to do in figure 6.4 below.

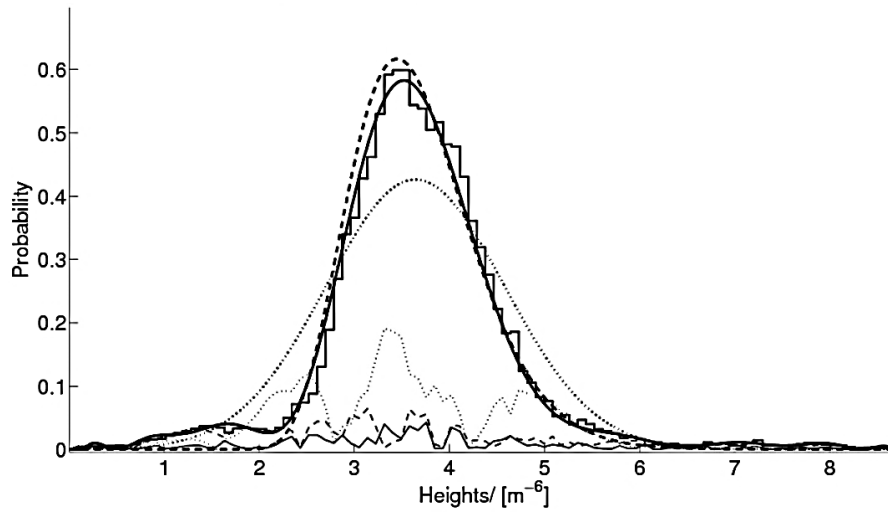


Figure 6.4. Aluminium-Aluminium interface composite surface height distribution. Same line styling definitions apply as in the previous figures, with the absolute error plotted as well.

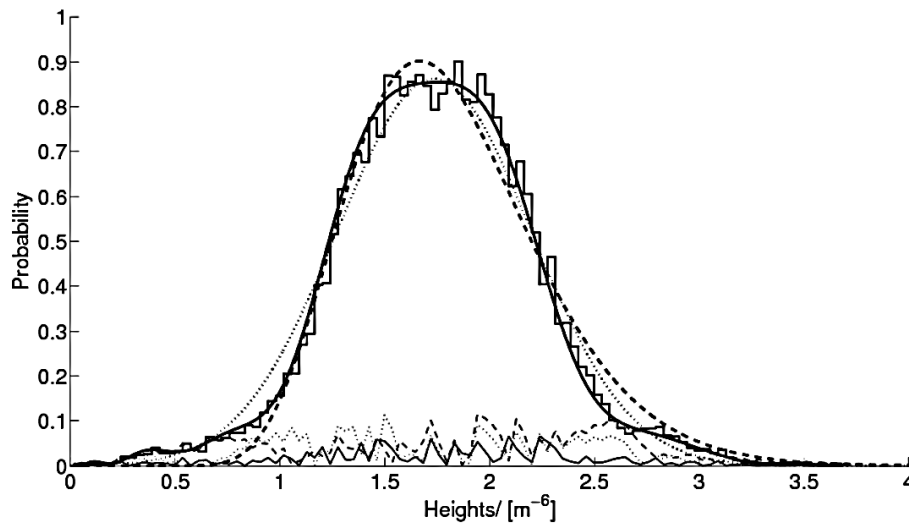


Figure 6.5. Aluminium-PMMA interface composite surface height distribution. Same line styling definitions apply as in the previous figures, with the absolute error plotted as well.

Distribution Fitting Error

In order to compare the effectiveness of each of the three distributions used to model the surface height data, a brief analysis of their individual error in describing the actual recorded results was carried out and the results are summarised in figure 6.6. The mean, median and maximum errors of the distributions were considered and averages were taken for each of the surface height distribution graphs in order to obtain a global mean, median and maximum absolute error which is plotted in figure 6.6 below.

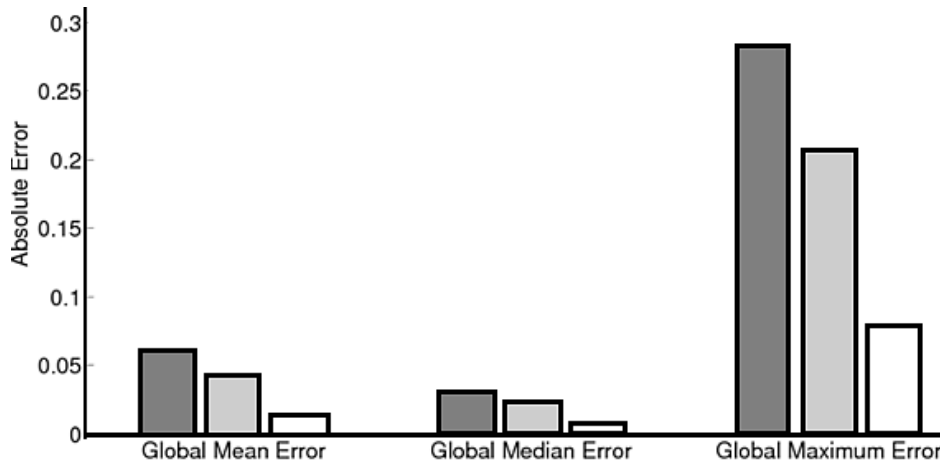


Figure 6.6. Bar chart showing the various measures of error of the fitting distributions used; Gaussian (dark grey), chi-squared (grey) and polynomial curve (white).

It is clear that the polynomial curve based distributions model the surface height data the best and therefore it is used in the parameter sensitivity analysis. It has roughly a third of the error in all three cases (mean, median and maximum) of measured error that the Gaussian distribution has, and nearly half the error of chi-squared distribution. The polynomial curve achieved this result as it was especially good at modelling the trailing ends as well as the most common heights, something which the Gaussian and to a lesser extent the chi-squared distribution could not do.

6.3 Static Modelling Results

Misalignment Correction Factor, ψ

In order to evaluate the multiplication constant, M (see equation 5.6) the misalignment correction factor, ψ had to be evaluated for the two static conditions modelled in this report.

The misalignment correction factor, ψ is plotted against the angle of contact, χ , in figure 6.7 A. In the two cases being investigated and modelled in this report the misalignment correction factor, ψ , can be assumed to be unity, since for misalignment up to 45 degrees in both interface conditions it remains around unity with 5% error. A similar value and conclusion was drawn by Baltazar, et al., (2002) when modelling aluminium-aluminium interfaces.

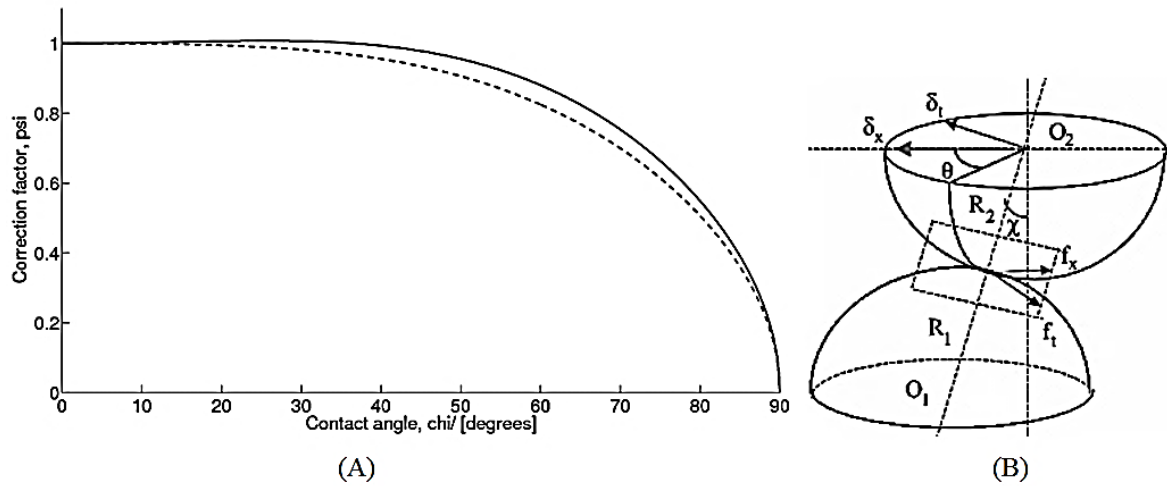


Figure 6.7. (A) Graph of how the misalignment factor , ψ varies with increasing misalignment angle of contact [degrees], χ for aluminium-aluminium (solid line) and aluminium-perspex interface (dashed line). (B) Diagram of the misalignment between two asperities (Yamada, et al., 1978) and (Brown & Scholz, 1985).

Static Modelling Results: Aluminium-Perspex Interface

The predicted nominal contact pressures and interfacial stiffnesses results using all three fitted distribution methods for comparison are plotted along with the experimental results of the aluminium-perspex interface (figure 6.8). The best approximation is given using the polynomial curve, then the chi-squared and finally the Gaussian distribution when solving equations 5.4 and 5.5 to obtain the nominal contact pressure and interfacial stiffness.

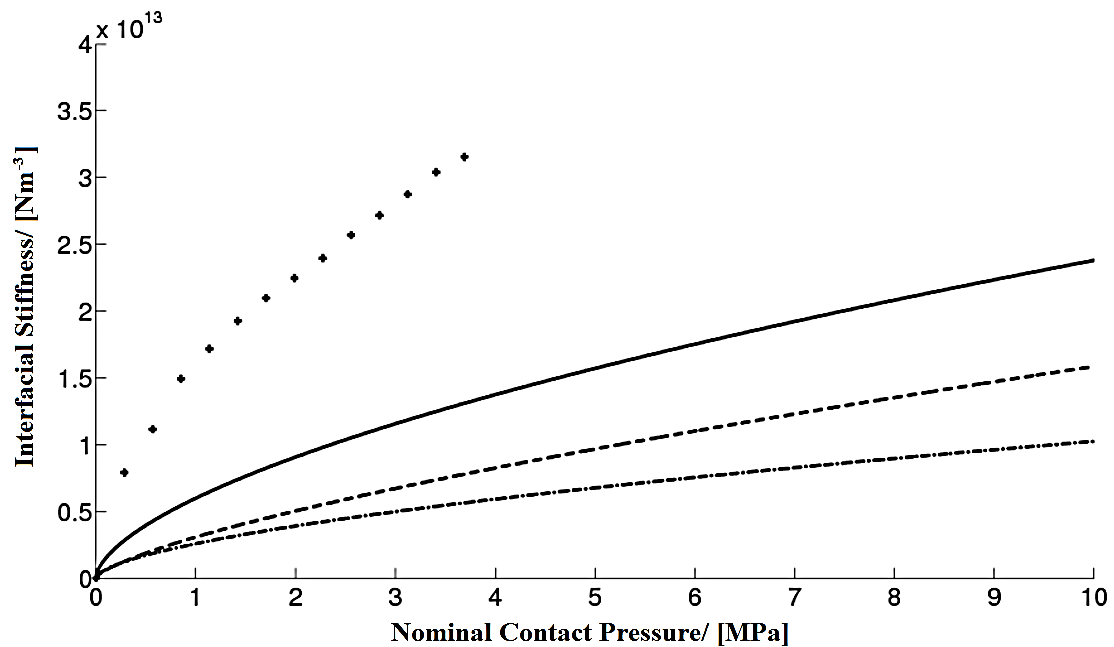


Figure 6.8. Graph comparing how the experimentally measured interfacial stiffness (converting measured reflection coefficient, RC , values using equation 2.6 and plotted as black diamond points) of the aluminium-perspex interface and the predicted static model results using the three statistical distributions; polynomial curve (solid line), chi-squared (dashed line) and the Gaussian (dotted line) vary with nominal contact pressure.

Predicted model results and the experimental results are plotted using the reflection coefficient instead of interfacial stiffness. Results from the static model were converted using equation 2.6 before being plotted alongside the experimental results in figure 6.9.

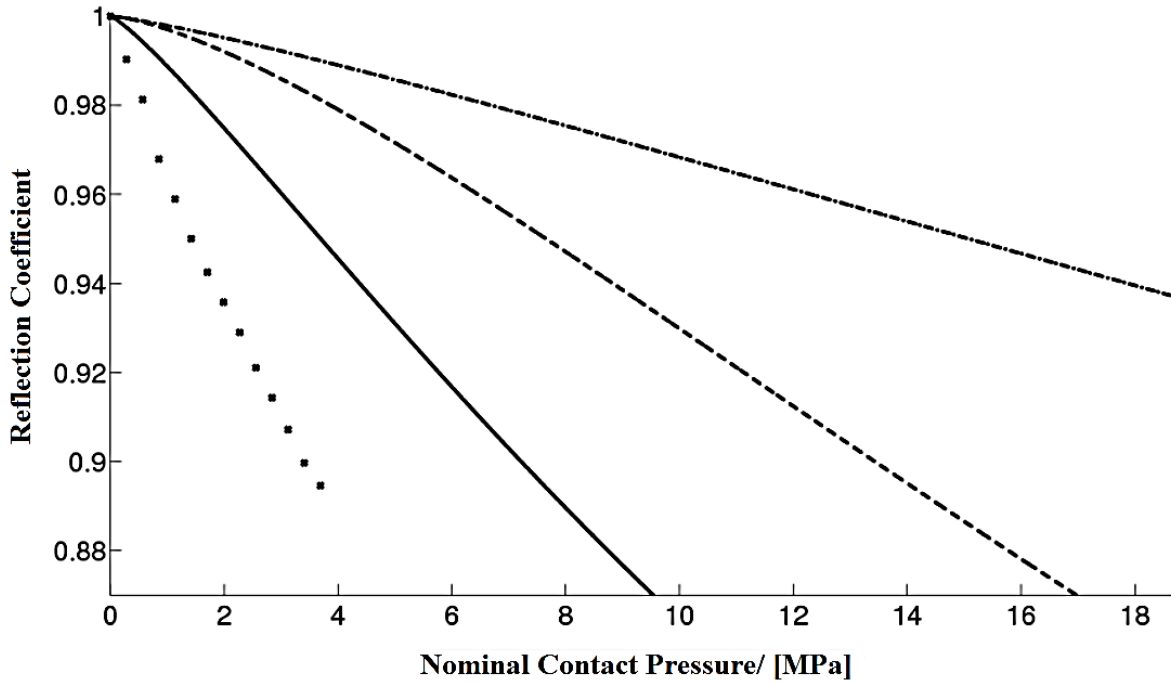


Figure 6.9. Graph comparing how the experimentally measured reflection coefficient, (black diamond points) of the aluminium-perspex interface and the static model results using the three statistical distributions; polynomial curve (solid line), chi-squared (dashed line) and the Gaussian (dotted line) vary with nominal contact pressure.

Static Modelling Results: Aluminium-Aluminium Interface

Results for the aluminium-aluminium interface are shown below in figures 6.10 and 6.11. The experimental values of the interfacial stiffness and the modelling results of the reflection coefficient were obtained using the appropriate rearrangements of equation 2.6.

As with the previous interface results, the polynomial based model best predicts the data. This can be attributed to the better fit it achieves of the measured surface height data. Overall, all three distributions better model the experimental results of the aluminium-aluminium interface than the previous aluminium-perspex interface. This could be due to the better modelling of the asperity diameters and the calculated equivalent Young's modulus, since both would affect the multiplication constant, M , see equations 5.4, 5.5 and 5.6 and therefore the results of the static model.

In both interface cases, the predicted nominal contact pressures seem to always be lower than the experimental results. It could be suggested that the surfaces have been deforming plastically against one another and so the profiles now better 'fit' together and therefore increasing the stiffness of the interface above the values predicted by the model. However, the applied pressure was never higher than 4.5MPa and the experiments lasted only for a couple

of minutes, suggesting that such severe plastic deformation and fitting of the surfaces was neither the sole nor the main reason for the recorded experimental results.

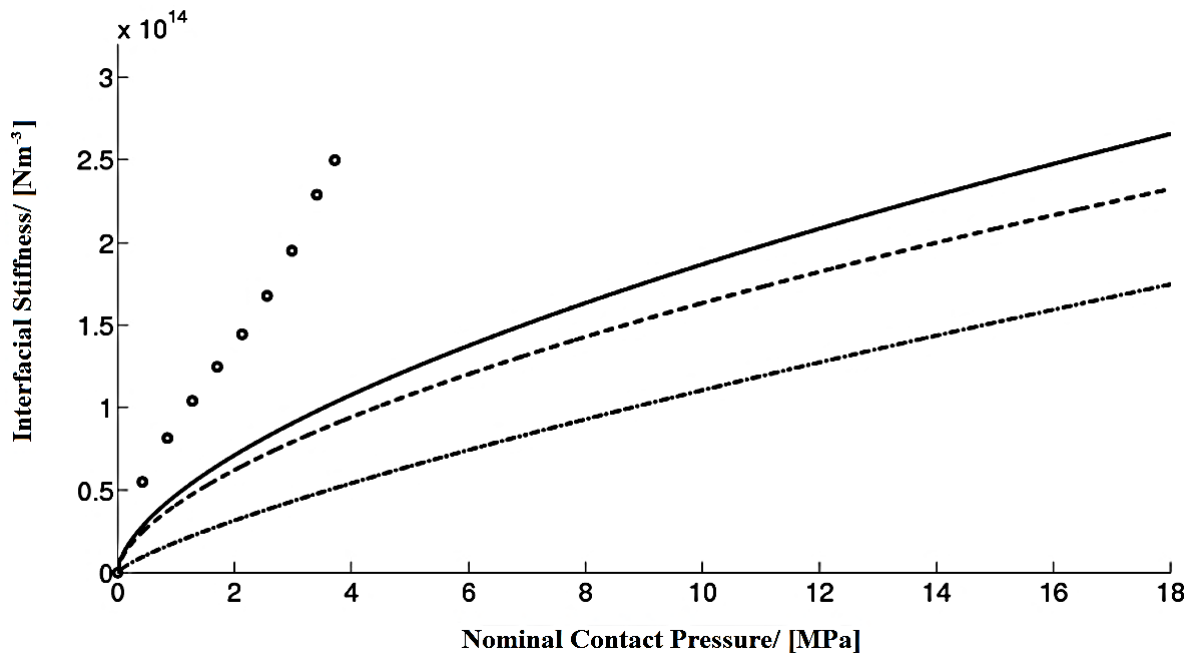


Figure 6.10. Graph comparing how the experimentally measured interfacial stiffness of the aluminium-aluminium interface and the static model results using the three statistical distributions; polynomial curve (solid line), chi-squared (dashed line) and the Gaussian (dotted line) vary with nominal contact pressure.

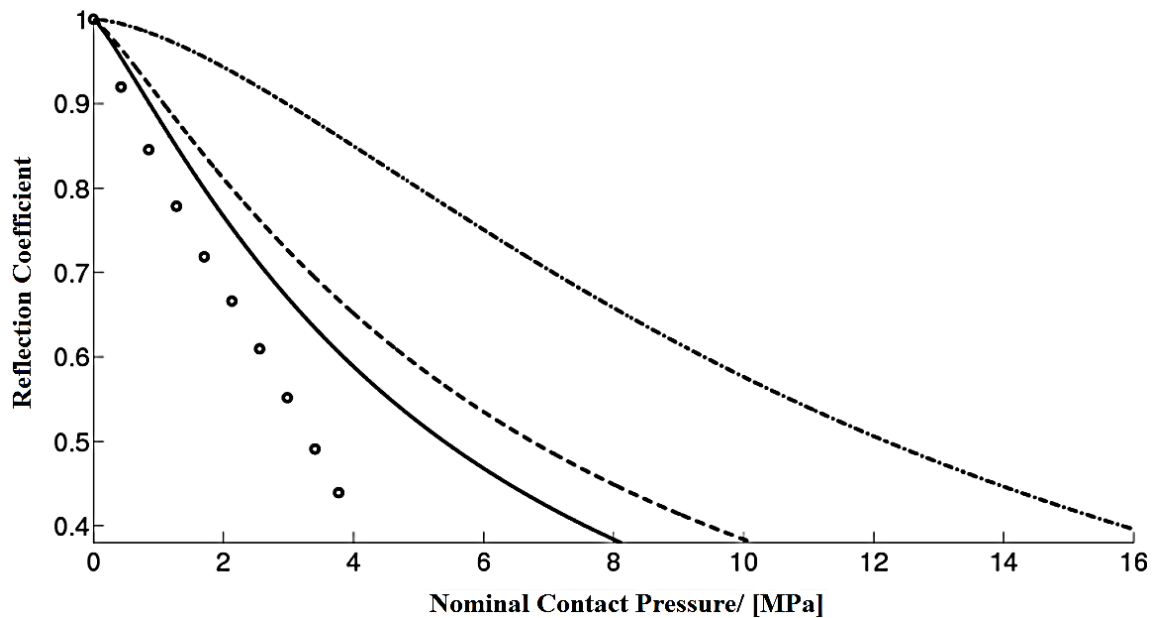


Figure 6.11. Graph comparing how the experimentally measured RC (circular points) of the aluminium-aluminium interface varies and the static model results vary with nominal contact pressure. All three distributions are plotted using the same line styling system of the previous figures.

The under predicting interfacial stiffness (and therefore over predicting reflection coefficient) nature of the model could be due to the chosen values of asperity diameter and equivalent stiffness (in the case of the perspex-aluminium interface).

6.4 Static Modelling Key Parameter Analysis

As discussed in the literature review, modelling procedure and static results sections, judging the average asperity diameter was not straight forward. A diameter of $0.5\mu\text{m}$ was originally chosen for all static models as this was the horizontal resolution of the surface profiler. In fact the asperity diameter could be a lot smaller. Several decreasing asperity diameters were chosen and the effects on the static model of the aluminium-perspex interface are shown below in figure 6.12. The polynomial curve distribution was chosen for this analysis since it gave the best approximation to the experimental results.

As the asperity diameter is decreased, better approximations of the experimental results were achieved. This suggests that the static model is rather sensitive to the chosen mean asperity values. The results suggest that the mean asperity diameter (assuming *ceteris paribus*) could in fact be approximately half of the originally used value ($0.227\mu\text{m}$ instead of $0.500\mu\text{m}$).

Greenwood & Williamson (1966) suggested that asperity diameters along the material surface could vary and be approximated by a Gaussian distribution. However, due to the fractal nature of surfaces, the definition of what is classed as a small or a large asperity is non-trivial and the experimental data is therefore hard to obtain to justify the hypothesis.

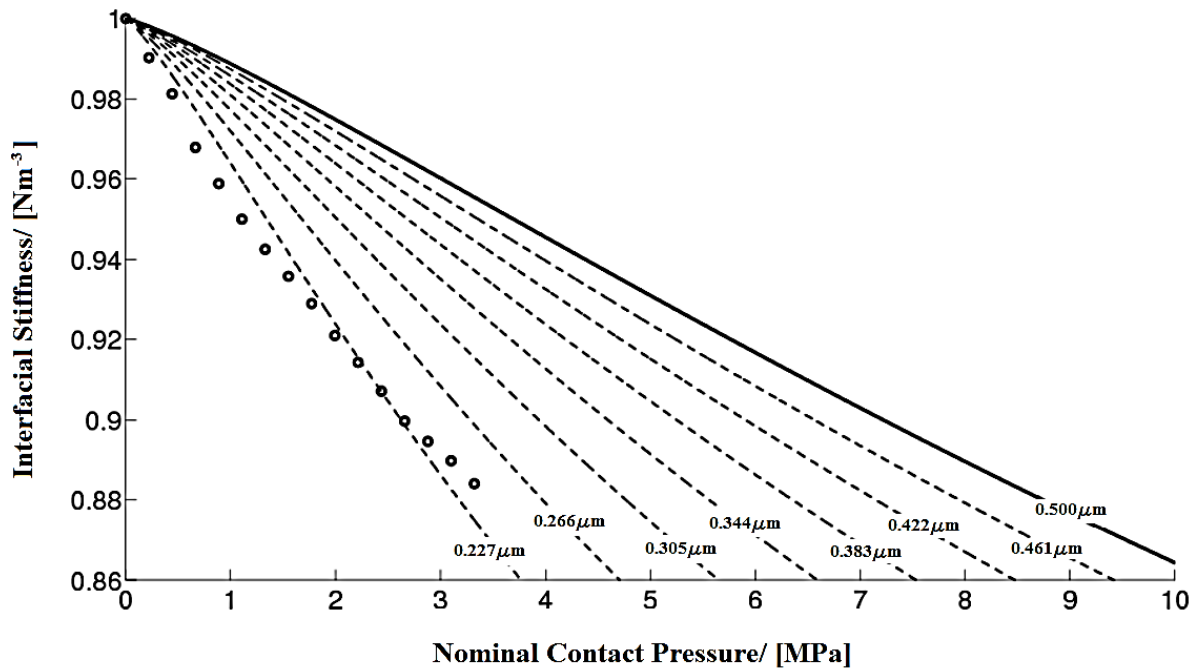


Figure 6.12. Graph showing how the static model varies when the asperity diameter is reduced (dashed lines) from the original value of the $0.5\mu\text{m}$ (result of the polynomial curve, solid line). The experimental results are plotted as circular points.

A similar procedure was applied to investigating the effects of increasing the value of the equivalent Young's modulus of the composite surface and the results are shown in figure 6.13. The results suggest that the true equivalent Young's modulus could be roughly 65-70% higher than previously calculated. The Young's modulus of either material could vary at the surface from the manufacturers data sheets.

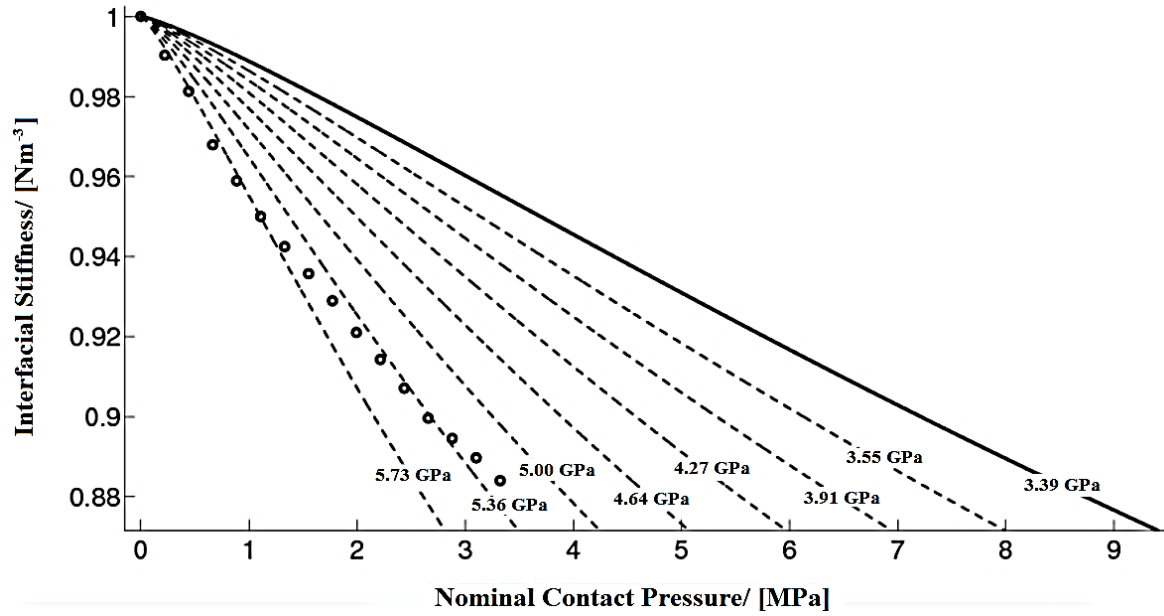


Figure 6.13. Graph showing how the static model varies when the equivalent Young's modulus is increased (dashed lines) from the original value of the 3.39GPa (result of the polynomial curve, solid line). for an aluminium-perspex interface. The experimental results are plotted as circular points.

6.5 Dynamic Modelling Results

Equations 5.10 and 5.13 were evaluated for Y using the approximate numerical method (described previously in section 5.2, and appendix section A3) and converted to reflection coefficient, RC , values using equation 5.9. The results are plotted below, figure 6.14. The reflection coefficient increases gently as the amplitude of the ultrasonic wave, U , is increased reaching a maximum value of $RC = 0.1079$, before springs are engaged at $U/d = 1$. Once the springs were engaged, RC increases rapidly to 0.6 at 25% compression of the springs.

Experimental results for comparison were not obtained due to the difficult assumptions imposed by the dynamic slip model. For example, a shear wave ultrasonic transducer where the amplitude can be freely changed is not common equipment. Secondly the model predicts values as the interface is slipping; as U increases until the frictional slip stress imposed at the boundary, τ_s , is overcome due to the energy and shearing motion of the wave. In reality these measurements are hard to obtain due to the rather instantaneous nature of slip at frictional boundaries.

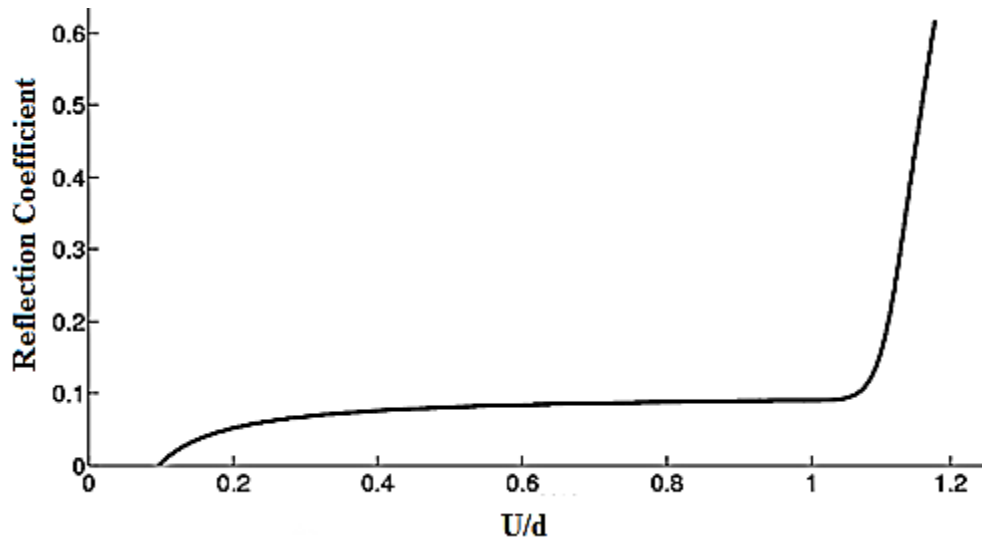


Figure 6.14. Graph of the dynamic slip model when applied to an aluminium-aluminium interface. Note that $U/d = 1$ is the point where the springs are initially engaged.

Results of the dynamic slip model when applied to an aluminium-aluminium interface agree with those predicted by Miller (1978). They also partially agree with the surface roughness parameters taken before and after the surfaces had been run on the test rig (see table 6.1 below). The surface roughness does change dramatically as both the mean surface roughness, R_A , and the root mean square, R_{RMS} , are roughly double those of the original ‘new’ surfaces. The experimental results were not obtained following the model guidelines (due to the strict assumptions the model imposes). The dynamically worn surfaces refer to surfaces that have been worn on the test rig from applying a constant pressure whilst increasing the rotating velocity of the aluminium or perspex test plate. The actual values are not directly comparable to the model results, what is more important is the difference of roughness between the surfaces before and after they had been run on the test rig.

Table 6.1. Summary of overall mean values of experimentally obtained surface profile parameters following the procedure and definitions outlined in figure 5.1.

	Surface Profile Parameters	
	$R_A/[\mu m]$	$R_{RMS}/[\mu m]$
Aluminium surface before experiment	0.255	0.351
Dynamically worn aluminium	0.590	0.880
Perspex surface before experiment	0.244	0.313
Dynamically worn perspex	0.528	0.688

7. Conclusion

This investigation concerned the ultrasonic measurement of static and dynamic contact. The investigation took both practical and theoretical forms; developing a thorough knowledge of and implementing predictive static and dynamic models of rough contact and completing a comprehensive regime of practical experimentation.

Static Contact

The rough static contact model developed for this report was based mainly on the works of Greenwood & Williamson (1966), Tattersall (1973), Brown & Scholz (1985), Drinkwater, et al., (1996), Baltazar, et al., (2002) and Valadez & Dwyer-Joyce (2008). A series of modifications were suggested to the original model, such as the use of a polynomial fitting curve to give a more accurate representation of the recorded surface heights distribution than the previously used chi-squared and Gaussian distributions. The polynomial fitting curve on average reduced the error by more than a half of the previously assumed distributions.

The use of statistical based models to predict reflection coefficients and nominal contact pressures had reasonable success in being able to replicate experimental results. All of the predicted stiffness, reflection coefficients and nominal contact pressure results were within an order of magnitude and in the best of cases, within twenty per cent of the experimental results. An analysis of the effects of changing the assumptions relating mean asperity size and equivalent Young's modulus was undertaken. Results suggested that the mean asperity diameter was roughly 50% smaller than previously assumed. Similarly, the equivalent Young's modulus for the composite aluminium-perspex surface could be around 70% higher than previously assumed. The latter highlights the variation of material properties quoted by manufacturers.

Dynamic Contact

The theoretical research for the rough dynamic contact model was almost entirely based on the dynamic slip model introduced by Miller (1978). There is a distinct lack of knowledge surrounding rough dynamic contact models due their complexity and the computation time needed in order to obtain numerical results. A clear difference in terms of roughness and distribution of asperity heights was noted between dynamically and statically worn surfaces. This further highlights the complexity of modelling a dynamic contact as the surface is changing.

The dynamic slip model developed in this report suggested that contact between materials at slip would result in a higher reflection coefficient. This could be attributed to the changing surface roughness, increasing air gaps, thus reducing the ability of ultrasound to be transmitted across the boundary.

References

- Adams, R. D. & Drinkwater, B. W., 1999. Nondestructive testing of adhesively-bonded joints. *International Journal of Materials & Product Technology*, 14(5), pp. 385-398.
- Archard, J. F., 1957. Elastic Deformation and the Laws of Friction. *Proceedings - Royal Society*, A(243), pp. 190-205.
- Baik, J. M. & Thompson, R. B., 1984. Ultrasonic scattering from imperfect interfaces; a quasi-static model. *Non-destructive testing*, Volume 4, pp. 177-196.
- Baltazar, A., Rokhlin, S. I. & Pecorari, C., 2002. On the relationship between ultrasonic and micromechanical properties of contacting rough surfaces. *Journal of the Mechanics and Physics of Solids*, Volume 50, pp. 1397-1416.
- Brown, S. R. & Scholz, C. H., 1985. Closure of Random Elastic Surfaces in Contact. *Journal of Geographical Research*, Volume 90, pp. 5531-5545.
- Butler, B., Goodall, J., Java, R. & Zuberi, S., 2011. *Measurement of Friction Using Ultrasound*, Bristol: Unveristy of Bristol.
- Carbone, G., Scaraggi, M. & Tartaglino, U., 2009. Adhesive contact of rough surfaces: Comparison between numerical calculations and analytical theories. *The European Physical Journal*, Volume 30, pp. 65-74.
- Childs, T. H., 1973. The presence of asperities in indentation experiments. *Wear*, Volume 25, p. 3.
- Drinkwater, B. W., 2012. *Ultrasonics and Acoustics: Introduction Lecture Slides*, Bristol: s.n.
- Drinkwater, B. W., Dywer-Joyce, R. S. & Cawley, P., 1996. A study of the interaction between ultrasound and a partially contacting solid-solid interface. *Proceedings: Mathematical, Physical and Engineering Sciences*, 452(1955), pp. 2613-2628.
- Flicek, R., Hills, D. A. & Dini, D., 2013. Progress in the application of notch asymptotics to the understanding of complete contacts subject to fretting fatigue. *Fatigue & Fracture of Engineering Materials & Structures*, 36(1), pp. 56-64.
- Gonzalez-Valadez, M. & Dywer-Joyce, R. S., 2009. Asperity Creep Measured by the Reflection of Ultrasound at Rough Surface Contact. *Journal of Tribology - Transactions of the ASME*, 131(2), pp. 021410-1.
- Greenwood, A. J. & Williamson, J. B., 1966. Contact of nominally flat surfaces. *Proceedings Royal Society London*, 295(1442), pp. 300-319.
- Greenwood, J. A. & Rowe, G. A., 1965. Deformation of surface asperities during bulk plastic flow. *Applied Physics*, Volume 36, p. 667.

- Halmshaw, R., 1991. *Non-Destructive Testing*. 2nd ed. London: Edward Arnold.
- Harris, C. M., 2005. *Dictionary of Architecture and Construction*. 4th ed. New York: McGraw-Hill.
- Johnson, K. L., 1985. *Contact Mechanics*. 9th ed. Cambridge: Cambridge University Press.
- Kendall, K. & Tabor, D., 1971. An ultrasonic study of the area of contact between stationary and sliding surfaces. *Proceedings of the Royal Society of London, Mathematical and Physical Sciences*, Volume 323, pp. 321-340.
- Khadem, R. & O'Connor, J. J., 1969. Axial compression of an elastic circular cylinder in contact with two identical half spaces. *International Journal of Engineering Science*, 7(8), pp. 785-800.
- Krolkowski, J. & Szczepek, J., 1991. Prediction of contact parameters using ultrasonic method. *Wear*, Volume 148, pp. 181-195.
- Larson, B., n.d. *Non-destructive Testing*. [Online] Available at: <http://www.ndt-ed.org> [Accessed 25 January 2013].
- Miller, R. K., 1978. The effects of boundary friction on the propagation of elastic waves. *Bulletin of the Seismological Society of America*, 68(4), pp. 987-998.
- Murray, C., Andrews, T., Dickinson, Q. & Brian Siu, T. C., 2012. *Measurement of Friction using Nonlinear Ultrasound*, Bristol: University of Bristol.
- Pau, M., Aymerich, F. & Ginesu, F., 2001. Measurements of nominal contact area in metallic interfaces: a comparison between an ultrasonic method and a pressure-sensitive film. *Wear*, 249(1), pp. 533-535.
- Reddyhoff, T., Kasolang, S., Dywer-Joyce, R. S. & Drinkwater, B. W., 2005. The phase shift of an ultrasonic pulse at an oil layer and determination of film thickness. *Proc. IMechE*, 219(J), pp. 387-400.
- Rose, J. L., 1999. *The Ultrasonic Waves in Solid Media*. Cambridge: Cambridge University Press.
- Silk, M. G., 1984. *Ultrasonic Transducers For Nondestructive Testing*. Bristol: A Hilger Ltd.
- Tattersall, G. H., 1973. The ultrasonic pulse-echo technique as applied to adhesion testing. *Applied Physics*, D(6), pp. 819-832.
- Teidelt, E., Starcevic, J. & Popov, V., 2012. Influence of Ultrasonic Oscillation on Static and Sliding Friction. *Tribology Letters*, Volume 48, pp. 51-62.
- Valadez, M. G. & Dwyer-Joyce, R. S., 2008. On the Interface Stiffness in Rough Contacts Using Ultrasonic Waves. *Ingenieria Mecanica Tecnologia Y Desarrollo*, 3(1), pp. 29-36.

Wang, L., 2010. Fractal analysis of fracture surfaces in aluminium borate whisker-reinforced aluminium alloy 6061 composite. *Transactions Nonferrous Met. Soc. China*, pp. 461-466.

Yamada, K., Kagami, J. & Naoi, T., 1978. Mechanism of elastic contact and friction between rough surfaces. *Wear*, pp. 15-34.

Appendix

A.1. Wave Formula and Reflection Coefficient Derivations

Full, three dimensional wave equations where λ and μ are the Lamé constants

$$\begin{aligned}\rho \frac{\delta^2 u}{\delta t^2} &= (\lambda + \mu) \frac{\delta}{\delta x} \left(\frac{\delta u}{\delta x} + \frac{\delta v}{\delta y} + \frac{\delta w}{\delta z} \right) + \mu \left(\frac{\delta^2 u}{\delta x^2} + \frac{\delta^2 u}{\delta y^2} + \frac{\delta^2 u}{\delta z^2} \right) \\ \rho \frac{\delta^2 v}{\delta t^2} &= (\lambda + \mu) \frac{\delta}{\delta y} \left(\frac{\delta u}{\delta x} + \frac{\delta v}{\delta y} + \frac{\delta w}{\delta z} \right) + \mu \left(\frac{\delta^2 v}{\delta x^2} + \frac{\delta^2 v}{\delta y^2} + \frac{\delta^2 v}{\delta z^2} \right) \\ \rho \frac{\delta^2 w}{\delta t^2} &= (\lambda + \mu) \frac{\delta}{\delta z} \left(\frac{\delta u}{\delta x} + \frac{\delta v}{\delta y} + \frac{\delta w}{\delta z} \right) + \mu \left(\frac{\delta^2 w}{\delta x^2} + \frac{\delta^2 w}{\delta y^2} + \frac{\delta^2 w}{\delta z^2} \right)\end{aligned}$$

For the derivation of the reflection coefficient, RC,

$$u_i + u_r = u_t$$

The interface pressure of each wave is given by:

$$p_i = i\mu_1 k_1 A_i e^{-i\omega t}$$

$$p_r = i\mu_1 k_1 A_r e^{-i\omega t}$$

$$p_t = i\mu_2 k_2 A_t e^{-i\omega t}$$

The interface pressure at the boundary ($x = 0$) can be described as continuous

$$P_i + P_r = P_t$$

Can now be expressed in the form of acoustic impedances, $z = \rho c$

Substituting $\mu = \rho c^2$ and $k = \frac{\omega}{c}$ such that $\mu k = \rho c \omega = z \omega$ gives

$$RC = \frac{A_r}{A_i} = \frac{z_1 - z_2}{z_1 + z_2}$$

A.2. Experimental Procedure

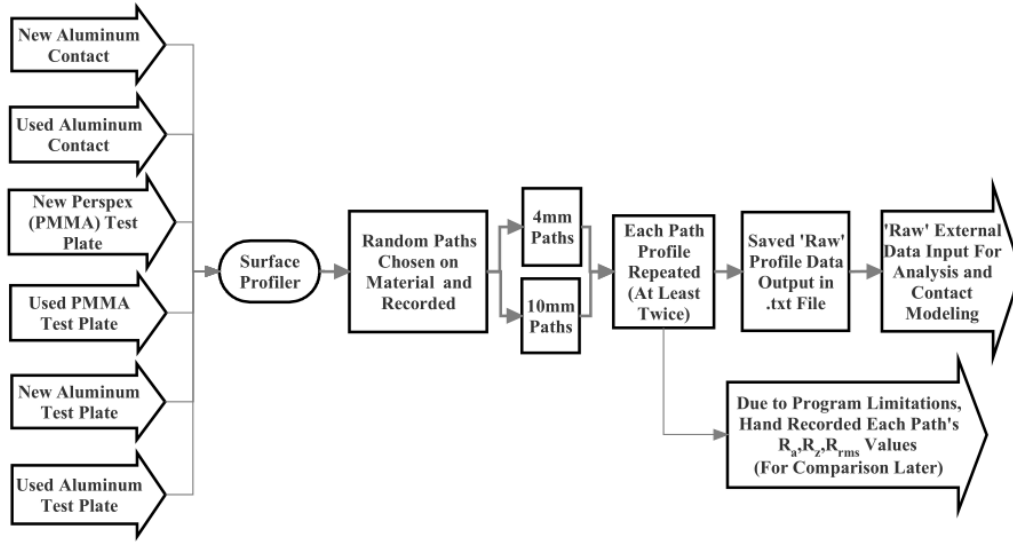


Figure A1. Block diagram of the surface profile data collection experimental process. Surface profiles were obtained from different materials and different surface conditions. Results were saved in a .txt file for later processing in MATLAB®.

A.3 Modelling Equations

Distributions

Chi-squared distribution (Baltazar, et al., 2002)

$$\chi^2 = \varphi(z_c) = \left[\frac{R_c}{\sqrt{2n}} \right]^{-0.5} \frac{z_c^{(n-2)/2}}{\Gamma(n/2)} \exp \left(-\frac{1}{2} \frac{z_c \sqrt{2n}}{R_c} \right)$$

Where n is the degrees of freedom of the distribution, Γ is the gamma function,

Gaussian distribution (Greenwood & Williamson, 1966)

$$\varphi(z_c, \mu, \sigma) = \frac{1}{\sigma \sqrt{2\pi}} \exp \left(\frac{-(z_c - \mu)^2}{2\sigma^2} \right)$$

Polynomial curve, order k

$$\varphi(z_c) = a_k z_c^k + a_{k-1} z_c^{k-1} + \dots + a_1 z_c + a_0$$

Dynamic Model

$$Y_{i+1} = \frac{-2ab \pm \sqrt{(2ab)^2 - 4(C^2(Y_i) + a^2)(b^2 - 4a^2U^2)}}{2(C^2(Y_i) + a^2)}$$

where,

$$C(Y_i) = 2kY/\pi \left\{ \cos^{-1} \left(d/Y_i \right) - 0.5 \sin \left(2 \cos^{-1} \left(d/Y_i \right) \right) \right\}$$

A.4. Height Distribution Results

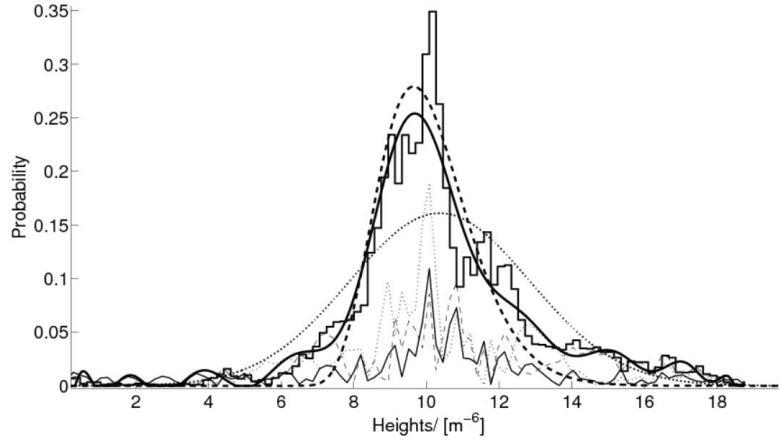


Figure A2. Height distribution data for dynamically worn aluminium test plate. The same line styling convection is used as in previous figures within this section.

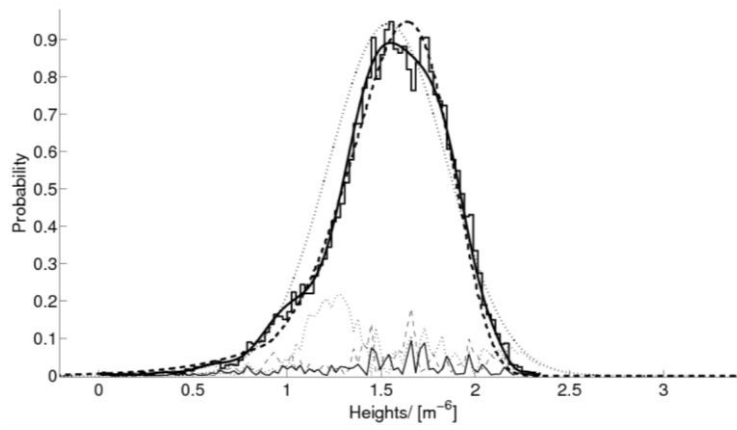


Figure A3. Height distribution data for statically worn perspex test plate. The same line styling convection is used as in previous figures within the results section.

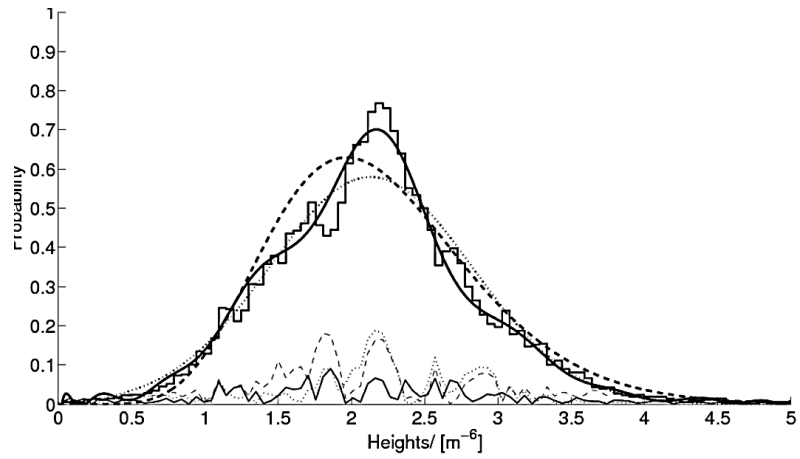


Figure A4. Height distribution data for dynamically worn perspex test plate. The same line styling convention is used as in previous figures within this section.

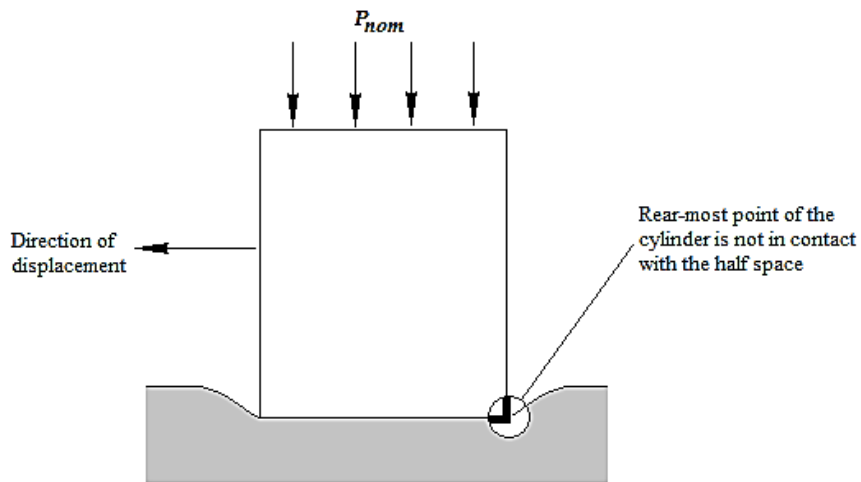
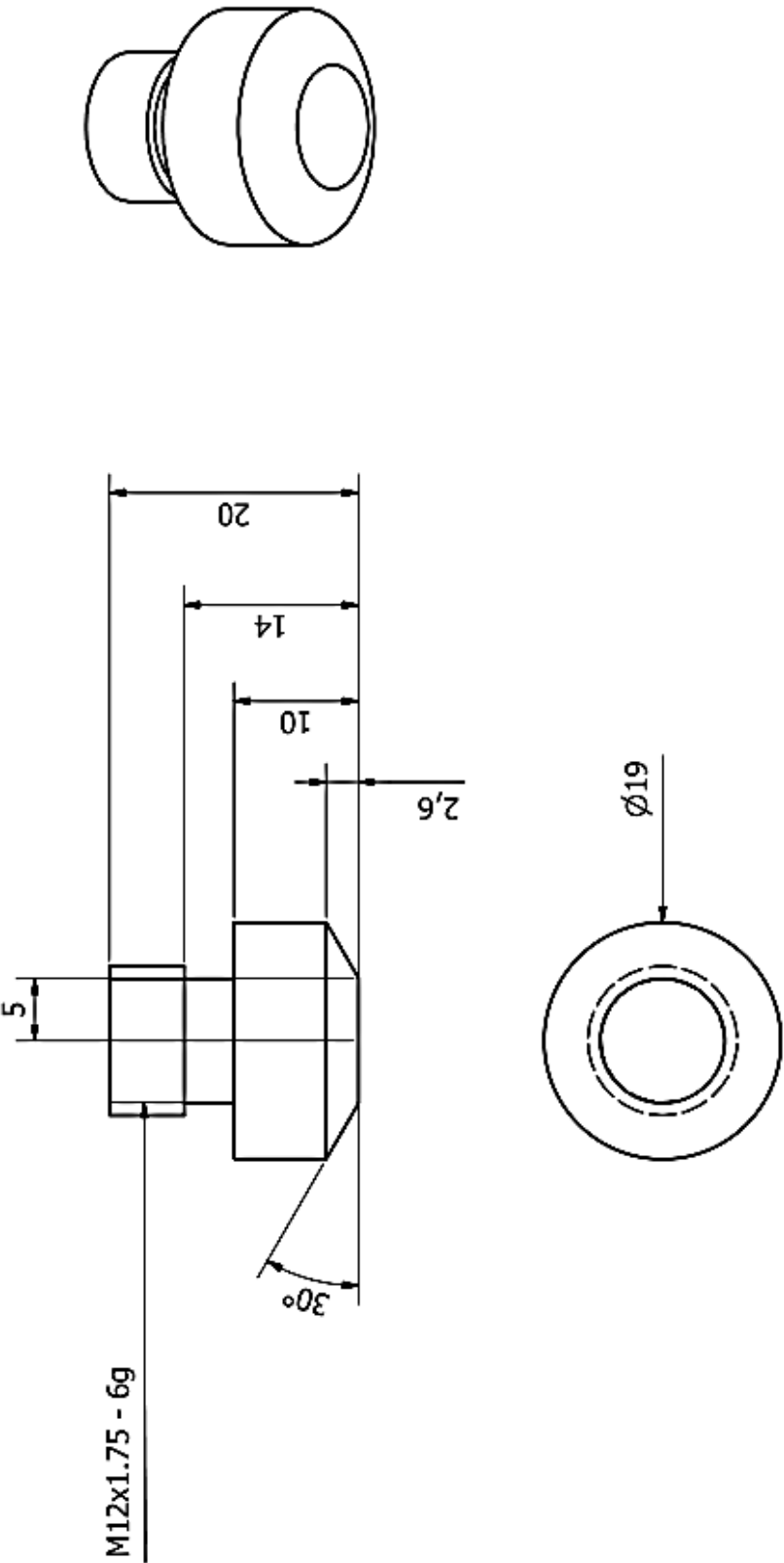


Figure A5. Diagram of the moving (fretting) punch with an elastic half space

A.5. Design Drawings

 <p>M12x1.75 - 6g</p> <p>30°</p> <p>5</p> <p>2,6</p> <p>10</p> <p>14</p> <p>20</p> <p>Ø19</p>	<p>PIETRO E CARNELLI</p>	<p>MATERIAL: Ø20 ALUMINIUM 6082t6 ALLOY BAR</p>
	<p>ULTRASONIC CONTACT 01/11/2012</p>	
	<p>ALL DIMENSIONS IN MM</p>	

